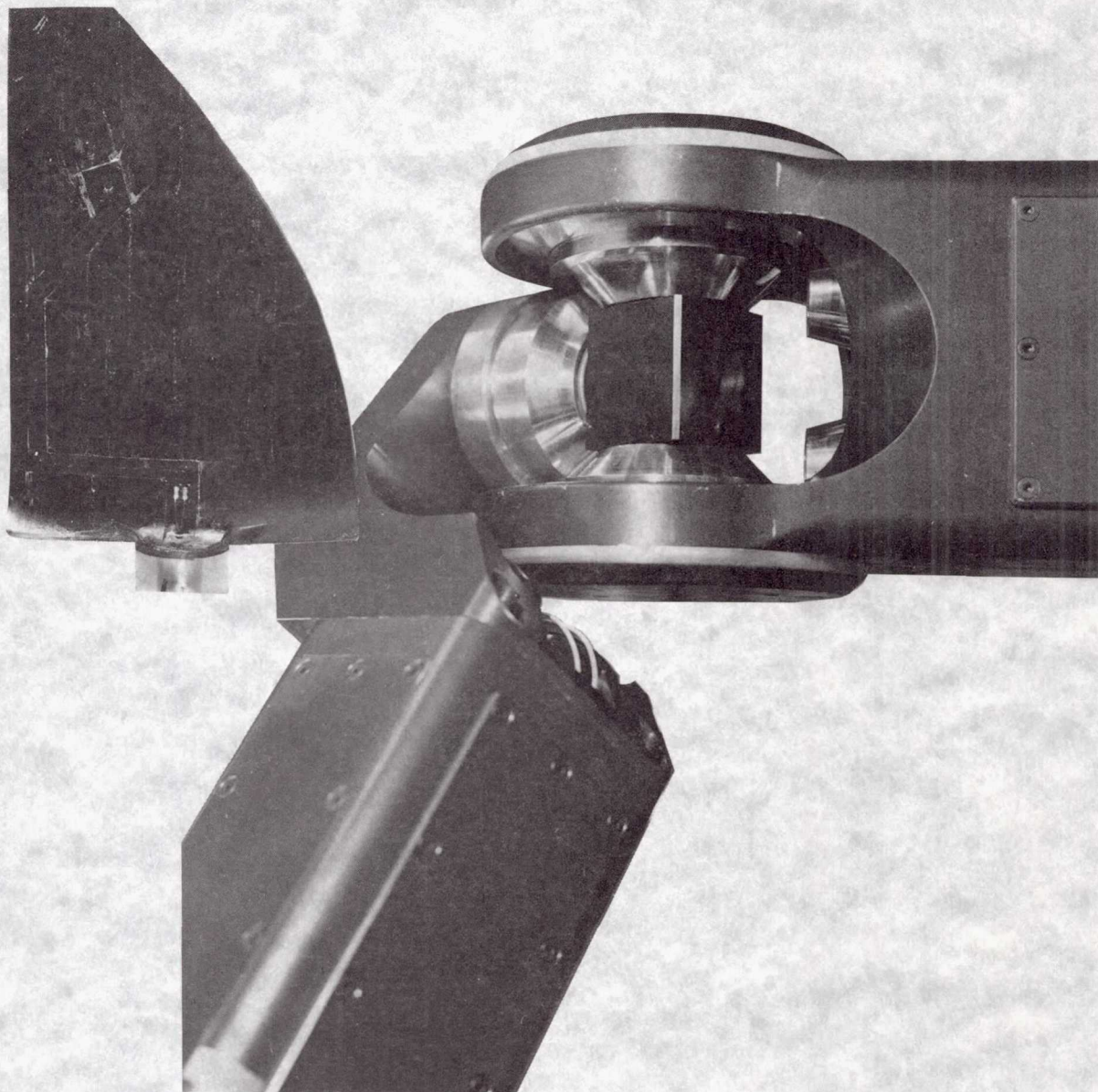


2-6-92  
E-5993

NASA Technical Memorandum 103747

# Structural Dynamics Branch Research and Accomplishments for FY 1990



**NASA**

November 1991  
Lewis Research Center

NASA Technical Memorandum 103747

# Structural Dynamics Branch Research and Accomplishments for FY 1990

*Lewis Research Center  
Cleveland, Ohio*

November 1991



National Aeronautics and  
Space Administration

**Scientific and Technical  
Information Program**

Trade names or manufacturers' names are used in this report for identification only. This usage does not constitute an official endorsement, either expressed or implied, by the National Aeronautics and Space Administration.

## Preface

This document highlights some of the technical accomplishments of the Structural Dynamics Branch at the NASA Lewis Research Center for fiscal year 1990. Included is the work of our in-house researchers, contractors, and grantees as they have achieved significant results throughout the year.

The Structural Dynamics Branch conducts research dealing with advanced propulsion and power systems as well as precision mechanical systems. Our work directly supports NASA's longer term aeronautical and space system program goals. We support turboprop, space experiments, space shuttle main engine (SSME), National Aero-Space Plane, supersonic fan, Space Station Freedom, and space power programs. This work can be broadly classified into four major activities: turbomachinery aeroelasticity, turbomachinery vibration control, dynamic systems response and analysis, and computational structural methods.

In aeroelasticity, we are developing improved analytical and experimental methods for avoiding flutter and minimizing forced vibration response of aerospace propulsion systems. Work elements include classical (frequency domain) methods, time domain methods, computational methods for fluid-coupled structural response, experimental methods, and application studies (turboprop, turbofan, turbopump, and advanced core technology). We have maintained an increased emphasis on the problems associated the forced vibration response of SSME class turbomachinery blading and counter-rotating propfan systems. Also, we have directly supported the Navy in demonstrating the viability of propfan technology for use in cruise missiles.

In vibration control, we conceive, analyze, develop, and demonstrate new methods to control vibrations in aerospace systems to increase life and performance. Work elements include actively controlled structures, passive vibration control methods, computational methods for active vibration control, and application studies (vibration isolation, magnetic and piezo-actively controlled bearings, and cryoturbomachinery). This area continues to be a major focus for us. Methods for unbalance control, critical speed control, and direct control of transient instabilities in rotating equipment are being developed. Next year's report will contain new control algorithms and approaches for extremely low power consuming magnetic bearings as well as some initial investigations for pushing operational temperatures to 1000 °F.

Dynamic systems work is directed to analyzing and verifying the dynamics of interacting systems as well as developing concepts and methods for motion control in microgravity environments. Work elements include space mechanisms, computational methods for dynamics analysis, and application studies (space lab mechanisms and robotics, NASP engine sealing concepts, and parallel computing for dynamics analysis). Our NASP engine sealing design work won an R&D 100 award as one of 100 most significant international research accomplishments last year. We have initiated a program to develop extremely long life rolling element bearings for space service and to establish requisite tools for designers.

Our work in computational methods is not considered a separate activity. Rather, computational methods development has been folded in with the objectives of the three other major focus areas within the branch. The goal of this work is to fundamentally improve the use of modern computers for the solution of realistic structural dynamics problems, with a particular emphasis on parallel processing. In aeroelasticity, computational methods work is focused on time-domain solutions and coupled fluid structure interaction. In vibration control, the computational methods are focused on individual bearing control, hierarchical schemes for controlling the response of distributed elastic shaft systems, and magnetic vibration isolation of space experiment platforms. In dynamic systems, the focus is on new algorithms for structural dynamics analysis.

The Structural Dynamics Branch staff has maintained their tradition of technically excellent work. I am privileged and very proud to represent their contributions.

L.J. Kiraly  
Branch Manager

**Page intentionally left blank**

# Contents

Reduced-Order Models for Nonlinear Aerodynamics .....	1
Updated Flutter Analysis of Supersonic Fan Stator .....	2
Application of an Efficient Hybrid Scheme for Aeroelastic Analysis of Advanced Propellers .....	3
Three-Dimensional, Full-Potential Method for Aeroelastic Modeling of Propfans .....	5
Aeroelastic Stability Characteristics of the SSME HPOTP Turbine Rotor .....	7
Blade Aeroelastic Stability Analyses for Cruise Missile Counterrotation Propfan Models .....	9
Full-Potential-Solver Flutter Analysis of Cascades in the Time Domain .....	11
Experimental Investigation of Flutter of the Counter-Rotating Propfan .....	13
Euler Solver Flutter Analysis of a Supersonic Cascade in the Time Domain .....	15
Linearized Unsteady Aerodynamic Analysis for Turbomachinery Flutter and Forced Response .....	17
Actively Controlled Hydraulic Force Actuator .....	19
Verification of Cryogenic Dampers .....	20
Hybrid Magnetic Bearing for Cryogenic Applications .....	21
Active Vibration Control (AVC) Test Results .....	23
Active Vibration Control Theory .....	26
A Global Approach for the Identification of Structural Connection Properties .....	29
Contact Area Temperature Profile of an Engaging Sprag Clutch .....	31
Dynamic Substructuring by the Boundary Flexibility Vector Method of Component Mode Synthesis .....	32
MIMD (Multi-Input, Multidata) Parallel FORTRAN Configuration File Generator .....	33
Shape and Topology Optimization by the Homogenization Method (Verification Studies) .....	34
Appendix—Researchers .....	36
Bibliography .....	37

# Reduced-Order Models for Nonlinear Aerodynamics

A semi-empirical model was developed to predict unsteady aerodynamic forces on arbitrary airfoils under stalled and unstalled conditions. For this model, aerodynamic forces are modeled with second-order, ordinary differential equations for lift and moment with airfoil motion as the input. The fluid lift force has the characteristics of a damped harmonic oscillator because of the fluid's inertia, dissipation, and compliance. The airfoil motion is assumed to drive the fluid lift oscillator, and the driving terms have nonlinear as well as linear components. The pitching moment is also represented with this form of equation. The parameters in these equations are determined from comparisons with the Navier-Stokes solver airfoil load data for small-amplitude oscillatory motions. The model is then compared with the Navier-Stokes solver airfoil load data for large-amplitude oscillatory motions.

This model is then used to provide the aerodynamic loads input to a two-degree-of-freedom structural dynamics model. These coupled second-order, ordinary differential equations are solved with an implicit, linear, multistep method with a backward differentiation formula, also known as Gear's stiff method. For the study of the flutter behavior of a NACA 0012 airfoil at Mach 0.3, the time response for a two-degree-of-freedom structural-fluid system using these equations was compared with those from the Navier-Stokes solver and the classical incompressible potential flow model. The savings in computer time and memory requirement, due to this model, are significant in comparison with those for the methods based directly on the Navier-Stokes equations.

Flutter boundary as a function of initial angle of attack is plotted in figure 1. For angles less than  $10^\circ$ , a particular reduced velocity  $V^*$  gives stable oscillations. For  $V^*$  greater than this value, oscillations increase in amplitude, and for  $V^*$  less than this value, oscillations decay. The flow over the airfoil is fully attached for these initial angles of attack. For angles greater than  $10^\circ$ , oscillations are stable over a range of  $V^*$  instead of at one particular value. Below this range, oscillations decay, and above this range, oscillations grow. However, the range of  $V^*$  over which the limit cycle is observed is somewhat different for the two fluid dynamic models. Figure 2 compares the maximum limit-cycle

amplitude from the Navier-Stokes solver and the semi-empirical model. The results are similar qualitatively.

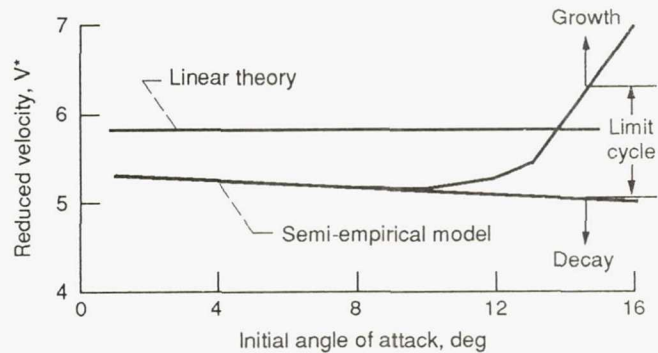


Figure 1.—Flutter boundary as a function of initial angle of attack.

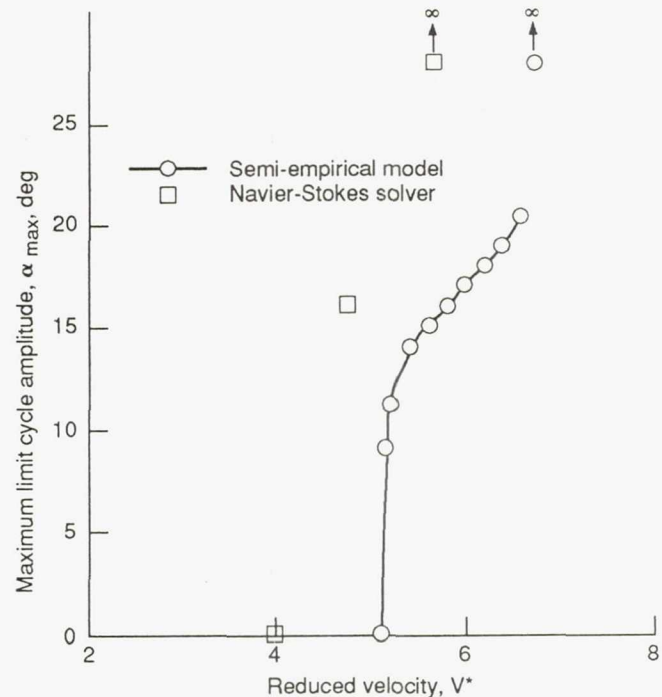


Figure 2.—Maximum limit cycle amplitude as a function of  $V^*$ . NACA 0012 airfoil, free-stream Mach number, 0.3; Reynolds number, 4 million; initial angle of attack,  $15^\circ$ .

---

**Researchers:** A.J. Mahajan (University of Toledo), K.R.V. Kaza (NASA Lewis), and E.H. Dowell and D.B. Bliss (Duke University).

## Updated Flutter Analysis of Supersonic Fan Stator

A flutter analysis for supersonic fans with supersonic axial flow was modified to include Lighthill's nonlinear piston theory. This modification allows us to represent the airfoil thickness and camber upstream of the shock impingement point on the airfoil. The code uses Lane's linear potential theory downstream of the shock impingement point, which represents the airfoil by a flat plate of zero thickness. Lane's potential theory was used over the full airfoil before this improvement.

The code was used to perform a flutter analysis of the NASA Lewis Research Center Supersonic Fan Stator 5. The stator design had been changed from a cantilevered end support to a pin-pin end support. The results of the flutter analysis are shown in figure 3. Two calculated flutter boundaries are shown, as well as the operating line for the critical stator mode, which is first torsion. The figure shows that the stator operating line is in the stable region for 0.2-percent structural damping but in the unstable region of 0.0-percent structural damping. Measurements show that the structural damping of a stator blade is greater than 1.4-percent for the first torsion mode. Therefore, the supersonic fan stator is predicted to be flutter free.

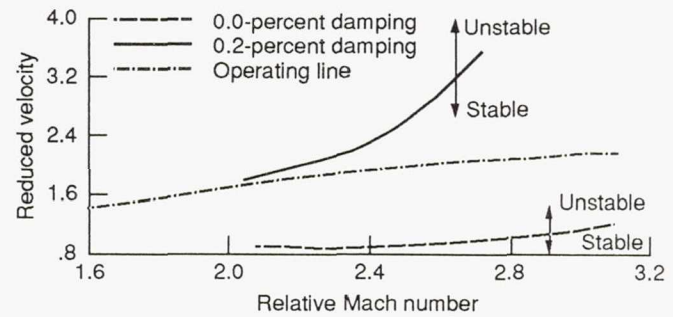


Figure 3.—Flutter boundary prediction for the NASA Lewis Supersonic Fan Stator 5 using Lighthill's nonlinear piston theory and Lane's potential theory.

---

**Researcher:** J.M. Lucero (NASA Lewis).

# Application of an Efficient Hybrid Scheme for Aeroelastic Analysis of Advanced Propellers

The aerodynamic and acoustic requirements of advanced propellers (propfans) have resulted in designs with thin, swept, and twisted blades of low aspect ratio and high solidity in comparison with conventional propellers. These propfan blades operate in subsonic, transonic, and possibly supersonic flows. The aeroelastic problem is inherently nonlinear because of large deflections caused by centrifugal and aerodynamic loads. Analytical aeroelastic models cannot account for nonlinear aerodynamics, real blade geometry (including thickness and camber), and flow incidence. However, high-speed computers and developments in numerical methods have made it possible to develop numerical models that can account for these effects.

A three-dimensional finite-difference solver based on Euler equations was formulated as a first step toward developing a numerical aeroelastic model. A hybrid solution scheme was adopted to reduce computational time in the aerodynamic load calculations. In this scheme, the fluxes in the radial direction are treated semi-explicitly, and the fluxes in the other two directions are treated implicitly. Example studies have shown that this did not affect the accuracy in comparison with a fully implicit scheme. In addition, the hybrid scheme requires only two inversions of the block tridiagonal matrix per time step instead of the three inversions for a fully implicit scheme. The hybrid scheme also reduces the computer memory requirements. Results from the performance calculations for an eight-bladed SR3 propfan correlate well with measurements and other analytical results.

The aerocode was interfaced with a finite element structural model (NASTRAN) to study the effect of structural flexibility on the propfan performance, and an aeroelastic iteration procedure (fig. 4) was developed. In this procedure, blade structural deflections with centrifugal loading are calculated for a given rotational speed, number of blades, blade setting angle, and given blade geometry (cold shape or shape at iteration 0). These deflections are added to the cold shape to get the blade shape at iteration 1. The aerodynamic load is calculated for this shape. The aerodynamic load on the aerodynamic grid is interpolated like the pressure load on the finite element grid. The blade structural deflections are

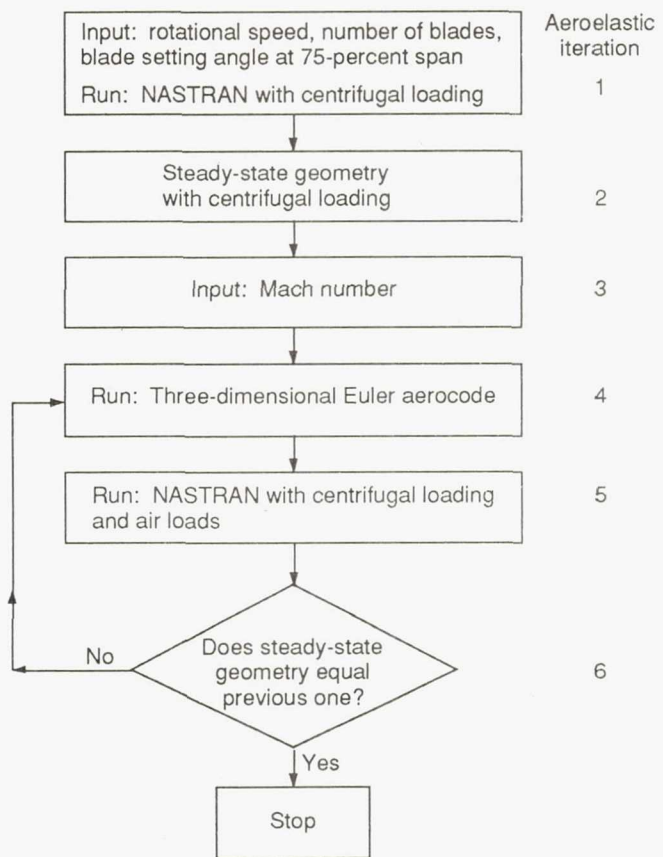


Figure 4.—Flow chart of aeroelastic analysis.

again obtained with the combined centrifugal and pressure loading. These deflections are transferred onto the aerodynamic grid to obtain a new shape for the aerodynamic load calculation. This process is repeated until the blade shape (steady state geometry), as indicated by the change in blade setting angle at 75-percent span, from two consecutive iterations, is within a given tolerance.

Figures 5 and 6 show static aeroelastic calculations performed for an SR7L propfan for a Mach number of 0.775 and an advance ratio of 3.088.

Figure 5 shows the variation of the blade setting angle at 75-percent span versus the iteration number. The centrifugal load decreases the blade setting angle from iteration 0 to iteration 1. The blade deflections due to the centrifugal loading are added to the blade shape at iteration 0 to get a new shape, and aerodynamic loads are calculated on this new

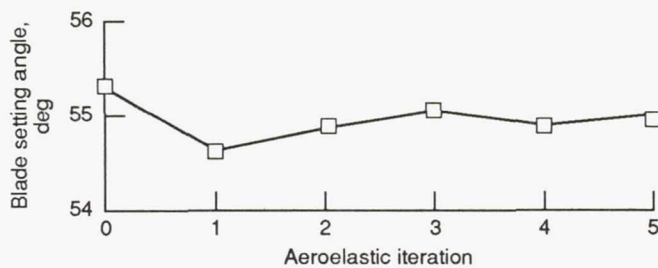


Figure 5.—Blade setting angle at 75-percent span versus aeroelastic iteration for SR-7L two-bladed propfan. Advance ratio, 3.088; Mach number, 0.775.

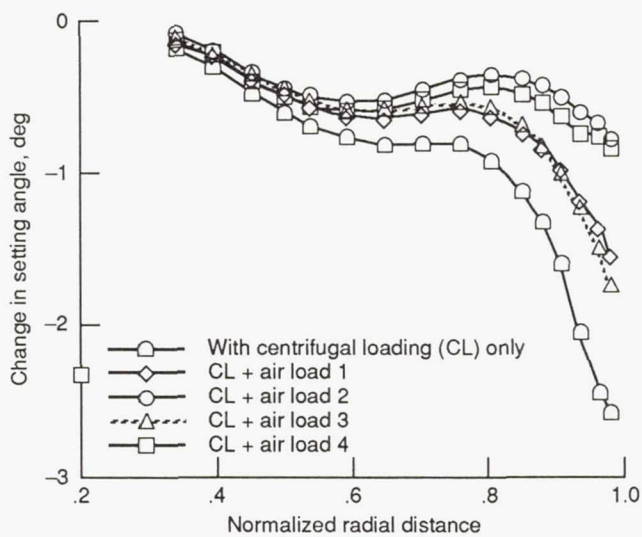


Figure 6.—Change in blade setting angle versus blade span for SR-7L two-propfan. Advance ratio, 3.088; Mach number, 0.775.

shape. These new loads are applied on the blade cold shape (shape at iteration 0) in NASTRAN to predict the new blade deflections with centrifugal and aerodynamic loads. Then, this procedure is continued until there is a small change in the blade setting angle. It can be seen that five iterations were required for convergence to the final blade shape.

In Figure 6, the relative change in blade setting angle over the span is plotted. The variation in the blade setting angle is nonlinear, and the largest deflection occurs near the tip, with practically no deflection at the root section. This shows that a rigid body rotation of the blade will not sufficiently account for the change in blade setting angle to produce accurate performance calculations.

---

**Researchers:** R. Srivastava and N.L. Sankar (Georgia Tech.), T.S.R. Reddy (University of Toledo), and D.L. Huff (NASA Lewis).

# Three-Dimensional, Full-Potential Method for Aeroelastic Modeling of Propfans

Propfans are designed to operate at high subsonic cruise (about Mach 0.8) with advance ratios around 3. At these conditions, the local Mach numbers vary from high subsonic at the hub to supersonic at the blade tip. Thus the flow over part of the blade is transonic. Linearized compressible theories are incapable of modeling shock waves that occur in transonic flow; therefore, a nonlinear aerodynamic model such as the full-potential model is required. The full-potential equation describes an inviscid, irrotational flow but neglects the entropy and vorticity generated by shock waves. In the flow conditions of interest, the shock waves are weak; that is, the jump in Mach number across the shock is small. Hence, the entropy and vorticity effects are negligible, and it is expected that the full-potential model will be sufficient to describe the important flow characteristics.

In the present study, the unsteady, three-dimensional, full-potential equation was solved with a finite-volume scheme. For this scheme, the solution is obtained with a time-accurate marching procedure. At each time level, a nonlinear problem is solved by a quasi-Newton iteration method. Approximate factorization is used so that only scalar tridiagonal systems of equations need to be solved. The internal iterations at each time level ensure temporal accuracy and conservation. A directional flux biasing scheme provides artificial viscosity in supersonic regions to capture compression shocks while excluding expansion shocks.

The aeroelastic equations that describe the motion of the blade are written in terms of in-vacuum free-vibration (normal) modes. At each time step, the blade displacements are used to calculate the grid around the blade that is used by the full-potential solver. This allows the blade motion to be fed into the aerodynamic solver and be used as a boundary condition.

The three-dimensional, full-potential solver was validated for steady calculation by comparison with experimental data for SR3 and SR7 blades. The results show good agreement, although some minor differences can be seen. These are attributed to the fact that the undeformed blade shape is used in the full-potential calculations, whereas the blade in the

experiment is deformed because of centrifugal and aerodynamic loads. Additional comparisons have also been made among results from the full-potential code, an Euler code, and a linearized-potential (panel) code. The results from the full-potential code show reasonable agreement with results from the panel code for low subsonic Mach numbers. In this flow regime, nonlinear effects are negligible, and the results are expected to agree. At higher Mach numbers, results from the linearized and full-potential codes show distinct differences due to the inability of the linearized theory to model transonic flow.

The aeroelastic stability can be calculated in two ways; these are briefly described. In the standard frequency domain flutter analysis, the blade displacements are assumed to be harmonic functions of time. This allows a complex eigenvalue problem to be formulated and solved; the eigenvalues determine stability. The generalized force derivatives that are required in the eigenvalue problem are determined from the full-potential solver. The blade is forced to deform in a single mode with displacement as a specified function of time (a pulse). The resulting generalized forces are stored as functions of time. The generalized force derivative at any given frequency is obtained as the ratio of the Fourier transforms of the generalized force and the blade motion.

In the alternative approach to stability analysis, known as the direct aeroelastic simulation, the aeroelastic equations are integrated in time together with the full-potential equation. Starting with a small initial perturbation, a predictor-corrector method integrates the aeroelastic equations. The blades show an oscillatory motion. The amplitude of motion either decays or grows in time, indicating stability or instability, respectively.

Aeroelastic stability calculations were made with both the frequency and time-domain methods described above for the eight-bladed SR3 rotor. The experiments showed that the rotor becomes unstable at Mach 0.65, 6000 rpm, and an interblade phase angle of 225°. This instability has been accurately predicted by the panel code. However, the full-potential code is currently restricted to zero

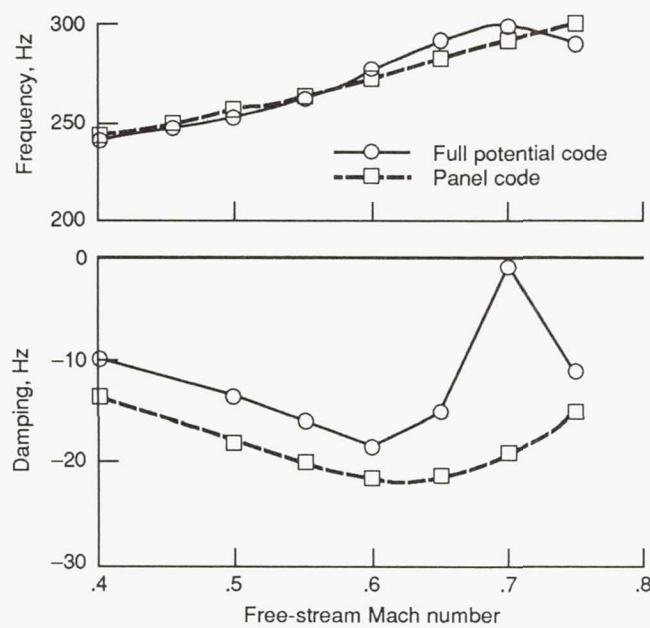


Figure 7.—Comparison of frequency and damping coefficients for SR3 blade. Advance ratio, 3.46; blade setting angle, 56.6°; interblade phase angle, 0°.

interblade phase angle motions. Therefore, code comparisons can only be made for stable conditions. Figure 7 shows the variation of frequency and damping with Mach number calculated using the full-potential and panel codes. As shown in the figure, the frequency predictions agree very well. The full-potential code results show systematically lower damping values, with a near neutral stability point at Mach 0.7, which is not present in the panel code results. The reason for this difference is currently being investigated. The predicted loss of stability near Mach 0.7 may or may not be a real nonlinear effect.

The main benefits of the three-dimensional, full-potential code are its ability to model nonlinear phenomena such as shock waves encountered in transonic flow and the capability to model the aeroelastic behavior of propfans in the frequency and time domain. Finally, the full-potential code requires less computational time and storage than for similar Euler codes even though it models all the flowfield characteristics that are considered important for the propfan.

---

**Researchers:** M.H. Williams (Purdue University) and G.L. Steffko (NASA Lewis).

# Aeroelastic Stability Characteristics of the SSME HPOTP Turbine Rotor

The space shuttle main engine (SSME) liquid oxygen high pressure oxidizer turbopump (HPOTP) turbine blade was analyzed dynamically, and the unsteady aerodynamic effect on the rotor stability was assessed. The method employed applies modal dynamic analysis to simulate the coupled blade/fluid system. A three-dimensional finite element model of the blade and its normal modes of vibration are used in conjunction with two-dimensional, linearized, unsteady aerodynamic theory. The aerodynamics are modeled by axisymmetric streamsurface strips along the blade span, and the blade structural and aerodynamic dynamic behaviors are coupled within modal space. Then, a complex eigenvalue problem is solved to determine the stability of the tuned rotor system.

The present analysis was applied to the SSME HPOTP first-stage turbine operating at the 109-percent rated-power level. For this blade model,

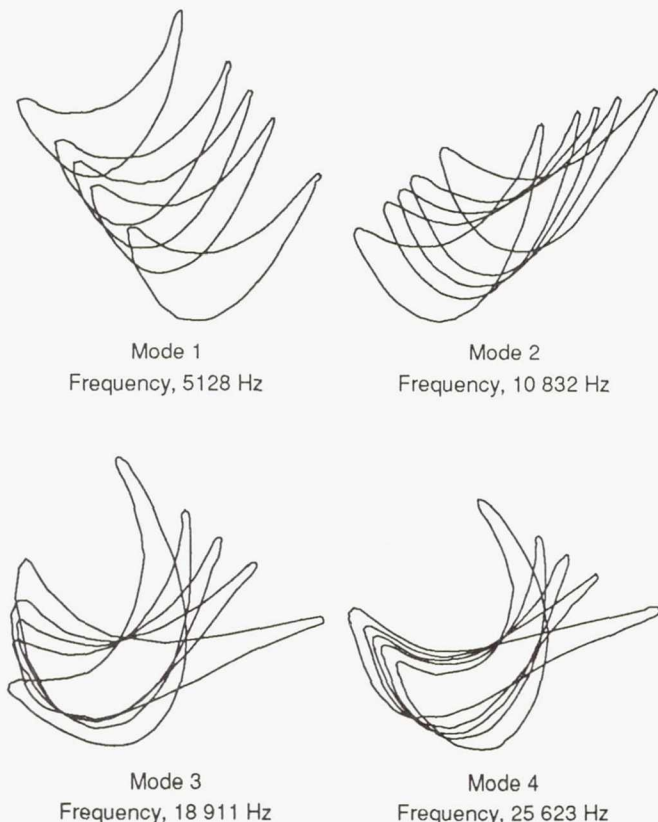
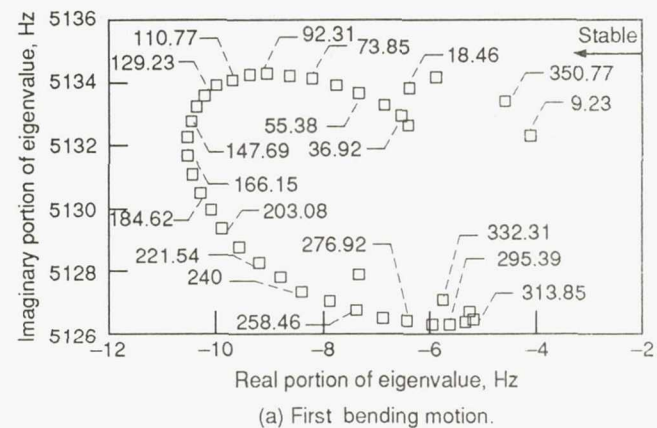


Figure 8.—Calculated mode shapes for high-pressure oxidizer turbopump (HPOTP) airfoil. Strip 1; radius, 5.17 in.



(a) First bending motion.

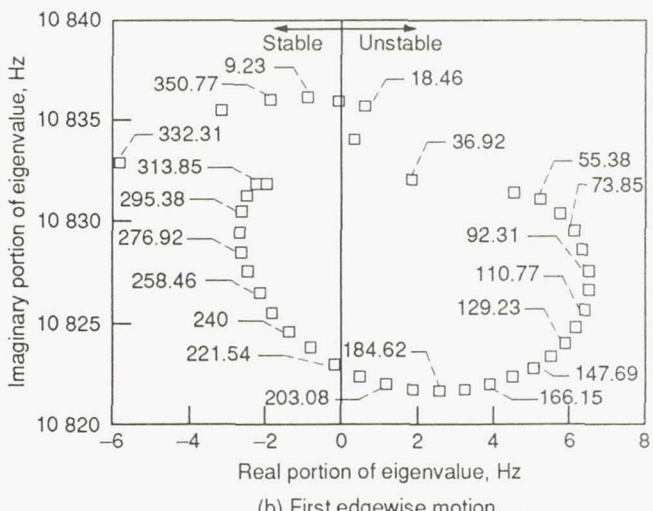


Figure 9.—Plot of root locus for tuned high-pressure oxidizer turbopump (HPOTP) turbine vibration. Numbers on plot indicate interblade phase angles.

six axisymmetric streamsurfaces along the airfoil span and were used, and the first four normal modes of the turbine blade were retained. Figure 8 shows a cross section through the airfoil indicating the first four calculated mode shapes near the blade tip. The aeroelastic computations with these modes determined that the aerodynamic damping levels were low (less than 0.5-percent of critical damping) for all modes of vibration. The second normal mode (edgewise mode) was found to be unstable for interblade phase angles from 18° up to 221°. The root locus of all calculated eigenvalues for motion in the first and second modes are included on figure 9. This analysis did not consider the effects of mechanical and material damping, which will have a stabilizing effect on the blade.

Blade cracking has been a continuing problem during the development of the HPOTP, although not as acute a problem since the introduction of blade-to-blade friction dampers at the blade platforms. The results from this analysis indicate that the history of blade cracking may be due to an unstable limit cycle vibration in the edgewise mode caused by flutter instability.

---

**Researchers:** T.E. Smith (Sverdrup) and G.L. Stefko (NASA Lewis).

# Blade Aeroelastic Stability Analyses for Cruise Missile Counterrotation Propfan Models

The ASTROP2 (Aeroelastic Stability and Response of Propulsion Systems) code was used to analyze the dynamic aeroelastic stability of three counterrotation (CR) propfan models in a 6-by-6 configuration for cruise missiles. This analysis supports a Navy-sponsored wind tunnel test in the NASA Ames 14-Foot Wind Tunnel. The purpose of the test is to investigate propfan/airframe interactions for cruise missiles.

Two of the propfan model blades were designed at NASA Lewis, and the third model was designed by the Garrett Corporation. One of the Lewis blade models, called CM1, is representative of a low tip speed, geared design; its tip diameter is 16.5 in. The other Lewis design, called CM2, is representative of a high tip speed, gearless design; its tip diameter is 14.25 in. In addition to aeroelastic stability, the Lewis designs had to satisfy aerodynamic performance and integral order structural criteria. Four organizations at Lewis, each in a different directorate, worked together to develop the Lewis designs. Multiple iterations were required before acceptable designs were found. The final Lewis designs are called CM1d and CM2d. The design furnished by Garrett had to be checked for aeroelastic stability only.

The ASTROP2 code is a modal analysis that uses a fully coupled motion, normal-mode structural model and a two-dimensional strip theory, unsteady cascade aerodynamic model. It is a frequency-domain solution that predicts the frequency, damping, and phase angle of the aeroelastic modes. The code is a single-rotor analysis. Hence, the forward and aft rotor of each CR model are analyzed separately. However, the analytical representation of the steady flow into each rotor includes the interaction between the rotors. This is the state-of-the-art for this type of analysis.

The analyses were performed at the blade design angle of each blade over the full range of tunnel operation conditions planned. This includes Mach numbers from 0.4 to 0.9, and rotor tip speeds from 450 to 850 ft/sec for the CM1 and Garrett blades and from 600 to 950 ft/sec for the CM2 blades. Typical dynamic stability analysis results for the three designs are shown in figures 10, 11, and 12. Each figure shows the damping variation with Mach

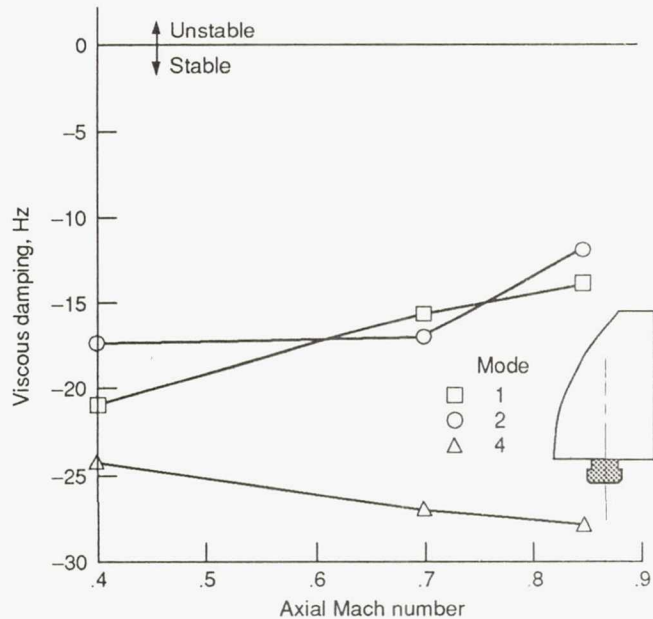


Figure 10.—0.55-scale-model aeroelastic stability prediction for CM1d forward six-bladed rotor. No steady airloads; tip speed, 750 ft/sec; blade setting angle at 75-percent span, 58°.

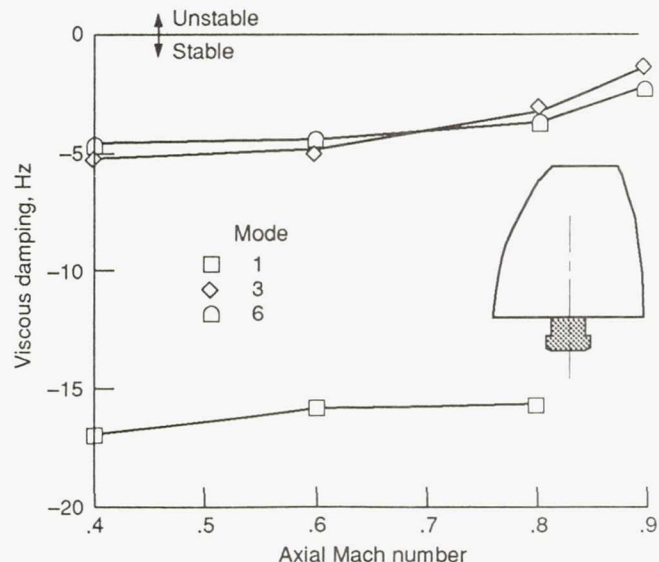


Figure 11.—0.55-scale-model aeroelastic stability prediction for CM1d forward six-bladed rotor. No steady airloads; tip speed, 750 ft/sec; blade setting angle at 75-percent span, 51.8°.

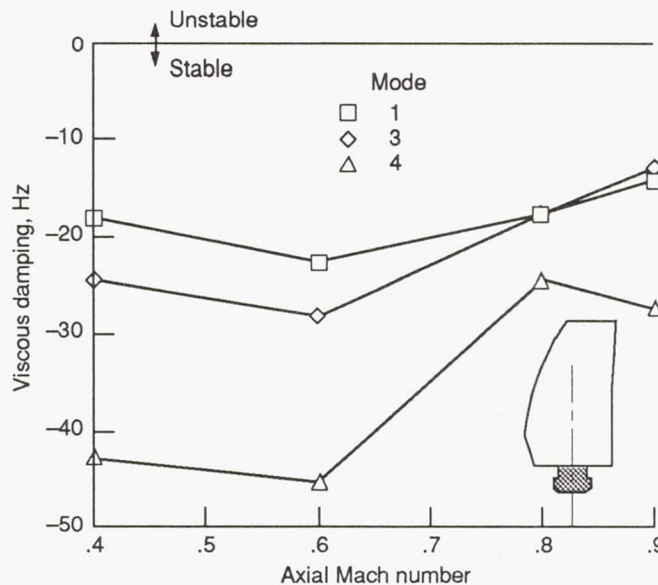


Figure 12.—0.55-Scale-model aeroelastic stability prediction for Garrett forward six-bladed rotor. No steady airloads; tip speed, 750 ft/sec; blade setting angle at 75-percent span, 64.0°.

number of only the three lowest damped blade modes, although six blade modes were used in the analyses. The figures show the blades remain in the stable region over the full Mach number range. These results are typical of all the conditions analyzed for CM1d, CM2d, and the Garrett forward and aft blades.

**Researchers:** J.M. Lucero (NASA Lewis), A.J. Mahajan (University of Toledo), and O. Mehmed (NASA Lewis).

# Full-Potential-Solver Flutter Analysis of Cascades in the Time Domain

Frequency domain analysis has been the traditional approach in flutter calculations of bladed disks (stators and rotors). However, this analysis is restricted to linear structural equations and aerodynamic forces that are linearly dependent on the blade displacements. Furthermore, the aerodynamic forces that are typically used with this approach are based on a linear potential theory which neglects the effects of blade loading due to thickness, camber, and angle-of-attack and is not suitable for transonic flows.

To overcome the restrictions of the linear aerodynamic theory, it is necessary to use governing fluid flow equations at a higher level of approximation. This precludes the use of simple semianalytical techniques and, instead, requires the use of advanced computational fluid dynamics (CFD) methods. The unsteady, full-potential equation is used in the present study as the basis for a two-dimensional cascade flow model that can represent flows over a wide range of Mach numbers from low subsonic to supersonic, including transonic flows with weak shocks. The computational method used to solve the full-potential equation is based on a time-accurate algorithm, and the time-domain method makes use of this fact. The equations of motion for the blades are integrated simultaneously with the full-potential equation governing the inviscid, irrotational fluid flow. In this approach, no a priori assumptions, such as the linear dependence of aerodynamic loads on blade motions, are necessary. Hence, nonlinear effects resulting from large amplitude motions can be treated without any difficulty.

In the present study, each blade of the cascade is allowed to have two degrees of freedom: pitching and plunging. The motion of each blade is described by two coupled governing differential equations representing the force and moment balance for each blade. The aerodynamic loads (lift and moment) that appear in these equations, resulting from the fluid flow around the moving blades, are calculated by integrating the pressure over the blade surfaces. The pressure distribution is, in turn, obtained from the potential function distribution that is obtained from the solution of the governing potential equation.

At the beginning of the time integration procedure, the steady flowfield is obtained for the specified

airfoil, given cascade geometry (stagger angle and gap-to-chord ratio), and specified inlet Mach number. Then one blade in the cascade is given a small disturbance in the form of a pitching velocity. The equations for the blades and the fluid are integrated in time to obtain the time history of the blade and fluid motions. The variations of blade pitching and plunging displacements with time are used to determine the stability of the cascade. These blade motions either decay or grow with time, depending on the value of reduced velocity  $V^*$  of the flow, indicating stability or instability, respectively. The reduced velocity is a nondimensional parameter based on the inlet flow velocity.

Calculations were made for a cascade with geometric and structural parameters that are representative of the SR5 propfan. The cascade has five blades, with a stagger angle of  $10.7^\circ$  and a gap-to-chord ratio of 1.85. The inlet Mach number considered is 0.7. Figures 13 and 14 show the typical response of the reference blade at stable ( $V^*=4.8$ ) and unstable ( $V^*=5.6$ ) conditions, respectively. The motions of the other blades in the cascade are similar and are,

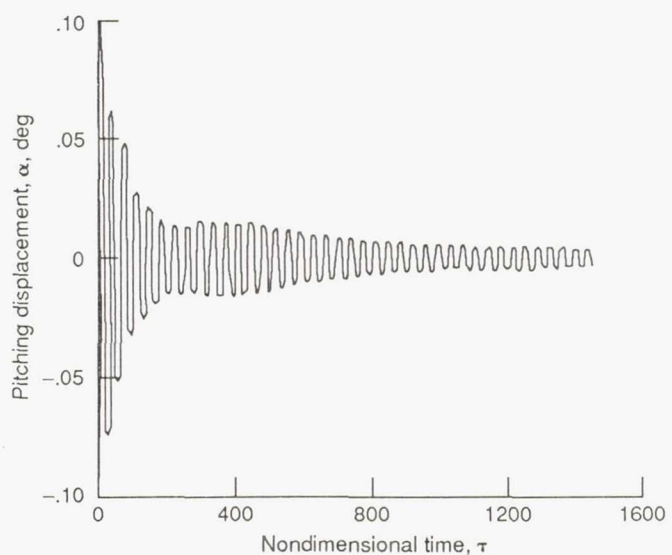


Figure 13.—Reference blade motion for stable blade response (reduced velocity,  $V^*$ , 4.8). Mach number, 0.7; stagger angle,  $10.7^\circ$ ; gap-to-chord ratio, 1.85.

therefore, not shown here. Also, the variation of plunging displacement, which is similar to the variation of the pitching displacement (figs. 13 and 14), is not shown. The displacements of each blade are curve-fitted as a function of time, allowing the damping to be calculated for the stable (positive damping) and unstable (negative damping) responses. The reduced velocity corresponding to zero damping ( $V^*_{f} = 5.2$ ) is obtained by linear interpolation. Similarly, the flutter frequency and the interblade phase angle at flutter are also calculated. Independent calculations have been made with the frequency-domain approach and full-potential theory. A comparison of the results (reduced velocity, frequency, and interblade phase angle at flutter) from the time-domain and frequency-domain methods show very good agreement for the example considered. Note that a linear structural model was used in this test case and that the amplitudes of the blades were restricted to the linear range to validate the time-domain method.

The main benefits of the time-domain approach are its ability to handle nonlinear structural models and aerodynamic forces that are nonlinearly dependent on blade displacements. Furthermore, the time-domain approach can realistically simulate the motion of the fluid and the cascade blades for a better physical understanding.

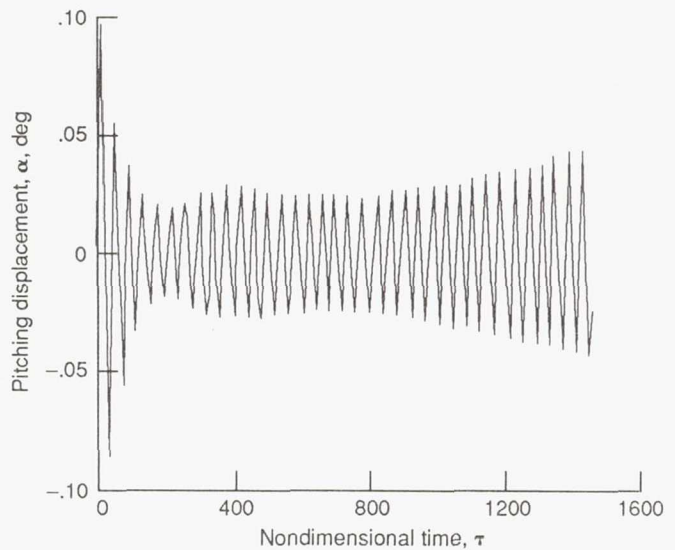


Figure 14.—Reference blade motion for stable blade response (reduced velocity,  $V^* = 5.6$ ). Mach number, 0.7; stagger blade response angle,  $10.7^\circ$ ; gap-to-chord ratio, 1.85.

---

**Researchers:** M.A. Bakhle, T.S.R. Reddy, and T.G. Keith (University of Toledo), and G.L. Steffko (NASA Lewis).

# Experimental Investigation of Flutter of the Counter-Rotating Propfan

Propfans have the potential to have unstalled flutter in their operating range. It is the thin airfoil sections, high blade sweep, high solidity, low aspect ratio, and transonic to supersonic tip speeds of propfans that give them this potential. Propfan unstalled flutter has been investigated experimentally, and flutter analyses have been developed for single-rotation (SR) propfans. However, several counter-rotation (CR) propfan models fluttered during aero-acoustic wind tunnel tests, and some trends and characteristics of the flutter were different from those observed for SR propfans. The present experiment was then planned with one of the CR propfan models, which had flutter of the front rotor, to guide the development of flutter analyses for CR propfans.

The main object of the experiment was to study the effect of the aerodynamic interactions between the rotors on the dynamic aeroelastic stability of the front rotor and to study the physics of the flutter. The installation of the model, called F21A21, in the NASA Lewis 8- by 6-Foot Supersonic Wind Tunnel is shown in figure 15. There are 13 blades on the front rotor and 10 blades on the rear rotor. The rotor diameters are nominally 2 ft. First, the front rotor was tested alone to map its stability. Then, both rotors were tested with the rear rotor at different power levels, and the front rotor stability was remapped to see the change. The stability map for the front rotor is shown in figure 16. The symbols show the conditions where the front rotor blades fluttered. Data are shown at three blade setting angles. The area below the lines through the symbols is the stable region of operation. The solid line is the boundary for the front rotor alone flutter conditions. The dotted line is the boundary for the front rotor flutter conditions with the rear rotor present but unpowered or windmilling. Comparing these two boundaries, we see that at most conditions the aft rotor increased the stability of the front rotor. So there is a favorable rotor aerodynamic interaction effect. The other open symbols are conditions where the rear rotor is powered, with increasing power

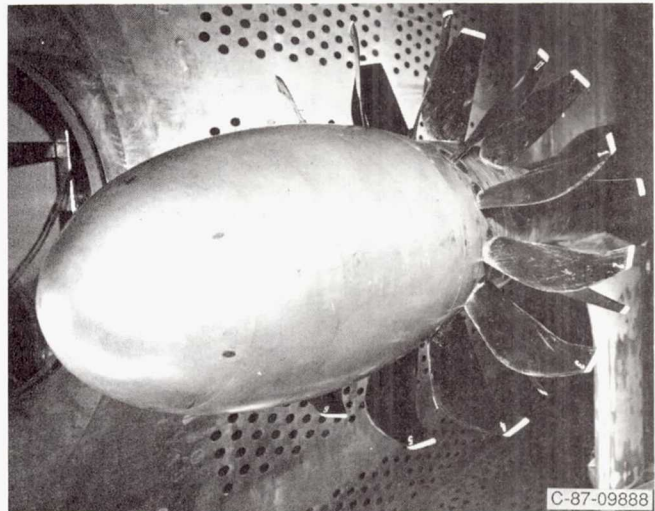


Figure 15.—F21/A21 Counterrotation propeller model in NASA Lewis 8-Foot by 6-Foot Supersonic Wind Tunnel.

moving toward the top of the figure. Again the data show a favorable effect of rotor aerodynamic interactions because the front rotor stability operating region has increased even further.

Figure 16 shows a strong dependence of blade setting angle. This trend is the same as observed with the SR propfan models and is caused by changes in aerodynamic coupling between the rotor blades and blade mode changes. However, the slope of the flutter boundaries in figure 16 does not agree with that observed with the SR models. For the SR models, as Mach number increased, the flutter rotor speed always decreased. Figure 16 shows an almost constant flutter rotor speed with increasing Mach number at two blade angles and shows an increase followed by a decrease at the third blade angle. The reason for the difference in this trend is being investigated.

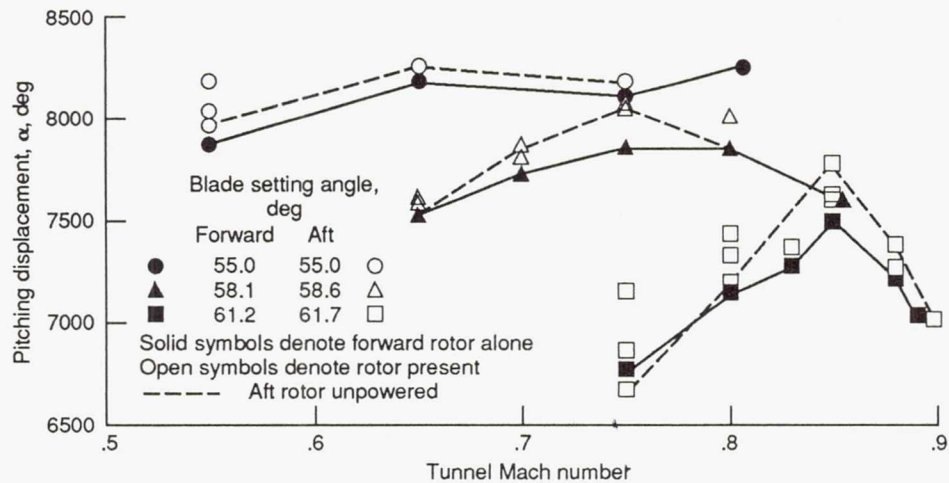


Figure 16.—F21 propfan flutter conditions for counterrotation model in 8-Foot by 6-Foot Supersonic Wind Tunnel.

---

**Researchers:** O. Mehmed and A.P. Kurkov (NASA Lewis).

# Euler Solver Flutter Analysis of a Supersonic Cascade in the Time Domain

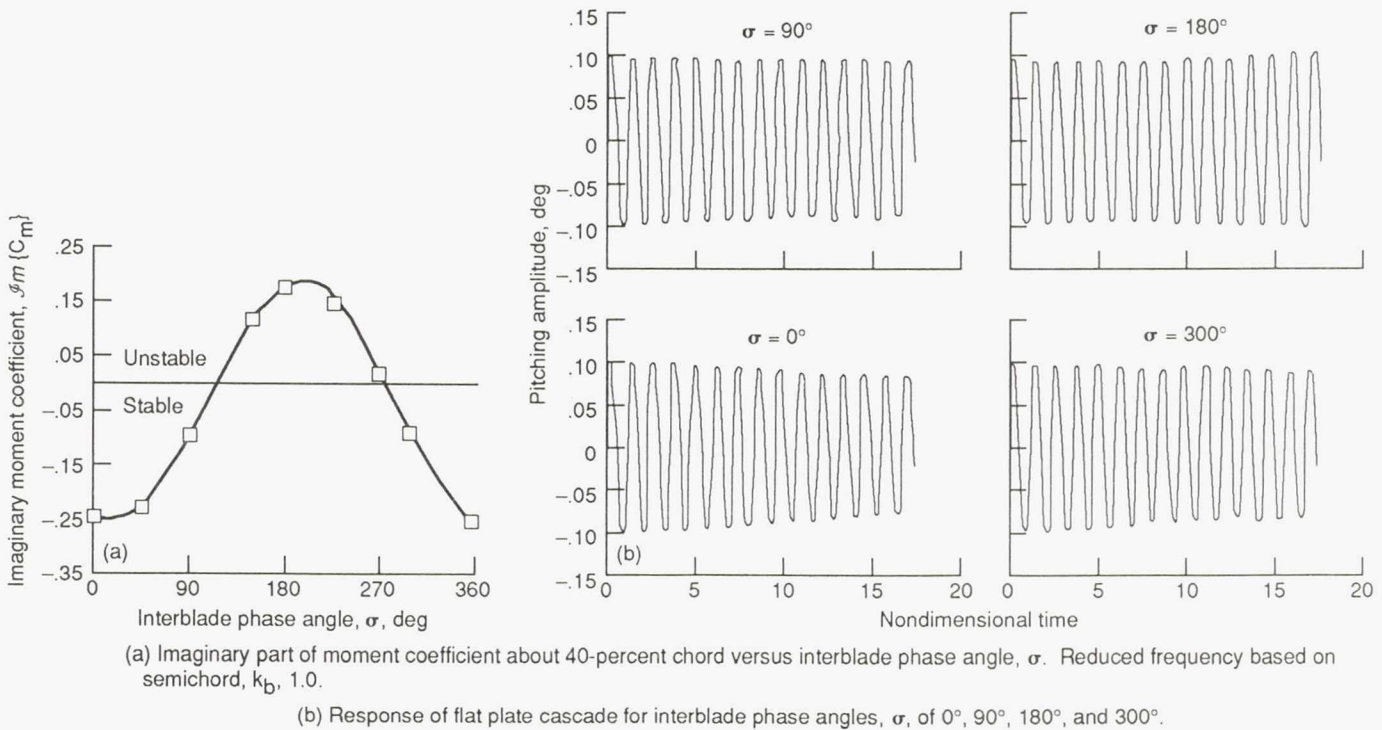
To evaluate the concept and potential of a supersonic throughflow fan (SSTF), NASA Lewis is currently conducting research to design, build, and test an SSTF. Understanding the aeroelastic behavior and identifying flutter boundaries are critical in such new designs. Many of the existing flutter analysis methods are based on linearized theories and are solved in the frequency domain. However, to incorporate both aerodynamic and structural nonlinearities, the aeroelastic equations have to be solved in the time domain. In addition, the aerodynamic model should be able to include the effects of thickness and camber and the effect of angle of attack in the analysis.

As a first step in developing a time-domain aeroelastic cascade code, the three-dimensional fan was modeled as a two-dimensional cascade of airfoils in supersonic axial flow. A finite difference code based on the Euler equations was combined with a typical section structural model with a

pitching degree of freedom. A deforming grid was used to specify the boundary conditions of the cascade during oscillation. The blade-to-blade phase lag (interblade phase angle  $\sigma$ ) in an oscillating cascade of blades was simulated by an appropriate choice of initial conditions.

Figure 17 shows a typical result obtained with the present time-domain aeroelastic code. The results are for an inlet Mach number of 2.61, a stagger angle of  $28^\circ$ , and a gap-to-chord ratio of 0.311.

Figure 17(a) shows the variation of the imaginary part of the moment coefficient ( $\text{Im} \{C_m\}$ ) with interblade phase angle  $\sigma$  for the flat plate cascade. The results were obtained from a frequency-domain solution. A reduced frequency based on semichord  $k_b$  equal to 1.0 was used in the calculations. When



(a) Imaginary part of moment coefficient about 40-percent chord versus interblade phase angle,  $\sigma$ . Reduced frequency based on semichord,  $k_b$ , 1.0.  
 (b) Response of flat plate cascade for interblade phase angles,  $\sigma$ , of  $0^\circ$ ,  $90^\circ$ ,  $180^\circ$ , and  $300^\circ$ .

Figure 17.—Flutter calculations for a supersonic cascade. Inlet Mach number, 2.61; stagger angle,  $28^\circ$ ; gap-to-chord, ratio, 0.311.

$\text{Im} \{C_m\}$  became positive, the moment led the motion of the flat plate and represented an unstable condition. The blade was unstable for  $\sigma$  between  $110^\circ$  and  $280^\circ$ .

For the problem analyzed, the ratio of the flutter frequency and the structural frequency is nearly one. Then the reduced velocity  $V^*$  used in the time-domain formulation is equal to the reciprocal of the reduced frequency  $k_b$ . Therefore, to simulate the time domain characteristics, it is sufficient to show that the responses at various interblade phase angles are stable or unstable for  $V^* = 1.0$ . Figure 17(b) shows the response plots for  $\sigma = 0^\circ, 90^\circ, 180^\circ$ , and

$300^\circ$ . The corresponding solutions (in fig. 17(a)) are respectively stable, stable, unstable, and stable. As seen in figure 17(b), the response plots predict the expected behavior. This validates the time-domain aeroelastic code and the interblade phase angle. Flutter calculations were also performed for two supersonic airfoils.

---

**Researchers:** T.S.R. Reddy and M.A. Bakhle (University of Toledo) and D.L. Huff (NASA Lewis).

# Linearized Unsteady Aerodynamic Analysis for Turbomachinery Flutter and Forced Response

The objective of this research program is to develop theoretical unsteady aerodynamic models and a computer code (LINFLO) for predicting compressible unsteady inviscid flows through blade rows of axial-flow turbomachines. These analyses are required for understanding the effect of unsteady aerodynamic phenomena on the structural dynamic stability, reliability, and aerodynamic performance of such blading. The research effort is devoted mainly to low-speed turbomachinery such as the space shuttle main engine (SSME) turbopump turbines. Furthermore, this research will apply more generally to the prediction of flutter and forced response in turbomachinery fan, compressor, and turbine blading operating in the subsonic and transonic regimes.

The unsteady aerodynamic behavior of turbomachinery blading is strongly dependent on the steady aerodynamic flow surrounding the cascade. Blade rows of axial-flow turbomachines often consist of airfoils varying from very thin to thick cross sections, all with varying degrees of camber. Such blades operate in a nonuniform steady flow due to the effects of airfoil thickness and flow incidence entering the cascade.

The linearized unsteady potential formulation models the small unsteady disturbances occurring in the cascade as first-order perturbations of the flow variables in the mass, momentum, and energy conservation equations. The unsteady perturbations, which are due to blade motion or incident aerodynamic disturbances, are linearized about a nonlinear, isentropic, irrotational steady potential flow. Figure 18 includes an illustration of the excitations considered in this approach.

Special consideration must be given to flows in which the unsteady disturbance is due to aerodynamic excitations. These excitations may be due to low-frequency gusts, high-frequency wakes, or pressure waves. For subsonic or transonic flows containing weak shocks, the mean steady flow is irrotational and isentropic. Under these conditions, the inviscid conservation equations become greatly simplified. Some analytical expressions for the linearized inviscid equations use a splitting technique to study the behavior of vorticity and entropy gusts for flows which have a steady potential form. The

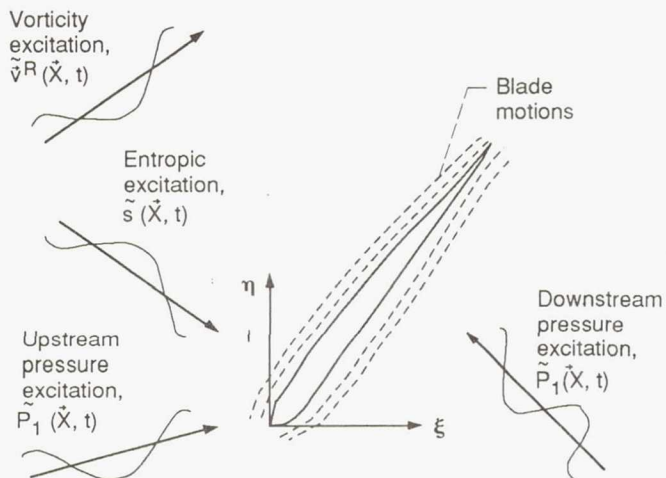


Figure 18.—Unsteady aerodynamic excitations due to blade oscillation and aerodynamic forcing functions.

unsteady velocity field is split into irrotational and rotational parts leading to three linear variable coefficient equations that are sequentially coupled, permitting their solution in order.

A distinct advantage of this formulation is that the unsteady behavior in a flow can be resolved very accurately with the linearized potential approach, at a greatly reduced computational effort. Figure 19 highlights an application to a low-frequency gust resulting from an inlet distortion passing by a cascade of thick, cambered airfoils. The computed unsteady surface pressure at the surface of the airfoils is shown, comparing a time-marching Euler computational fluid dynamics (CFD) code, a linearized Euler code, and the LINFLO linearized potential code. All three codes show excellent agreement for this case. Estimates of the computational time for each of the three codes show that the LINFLO calculations required several orders of magnitude less CPU (central processing unit) time than the other CFD codes.

The quick computational time for the unsteady aerodynamic response is extremely important from an aeroelastic analysis viewpoint. The effects of changes in Mach number and excitations along with blade-to-blade structural mistuning require a large number of computations for the aerodynamic forces.

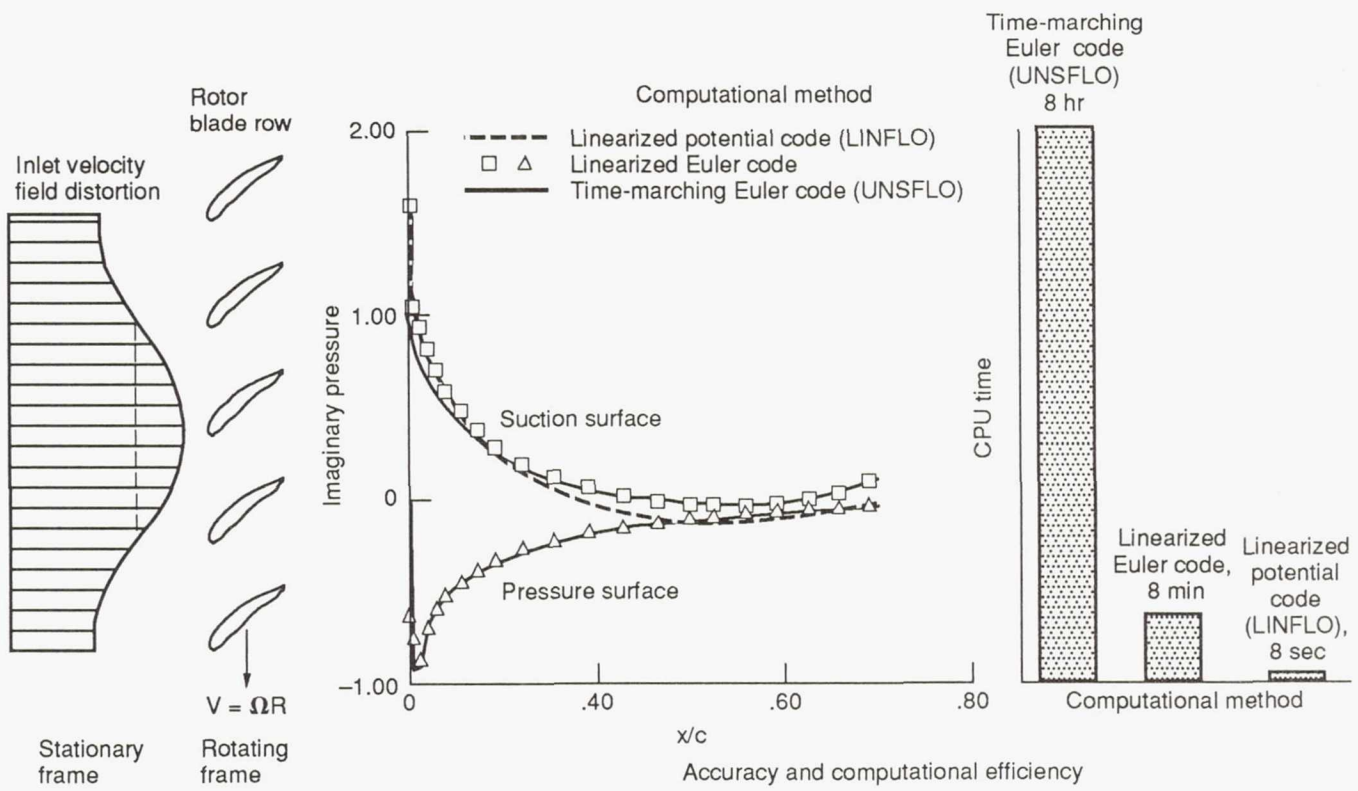


Figure 19.—Calculation of low-frequency gust response and comparison to similar computational fluid dynamics (CFD) methods.

**Researchers:** J. Verdon and K. Hall (United Technologies), T.E. Smith (Sverdrup), and G.L. Stefko (NASA Lewis).

# Actively Controlled Hydraulic Force Actuator

The hydraulic force actuator is a device that actively controls rotor vibrations by using hydraulic pressure to apply control forces to a rotor bearing housing. Figure 20 shows a schematic of the hydraulic force actuator system, and figure 21 is a photograph of the test rig. The rig consists of a mass which is free to move horizontally but constrained vertically. Hydraulic pressure is introduced into the pressure chambers on either side of the mass. The membrane which forms the inner wall of the chamber is very flexible and deflects under the action of the hydraulic pressure, thereby transmitting a force to the mass. The servovalve is in a closed-loop control system and controls the pressure difference in the chambers in response to electrical signal inputs. The control system can control either the amplitude of the mass or the force applied to it.

Figure 22 shows the frequency response and phase shift of the mass motion for a sinusoidal input to the servovalve of 0.0025-in. amplitude for frequencies up to 100 Hz. The gain in amplitude at 68 Hz is

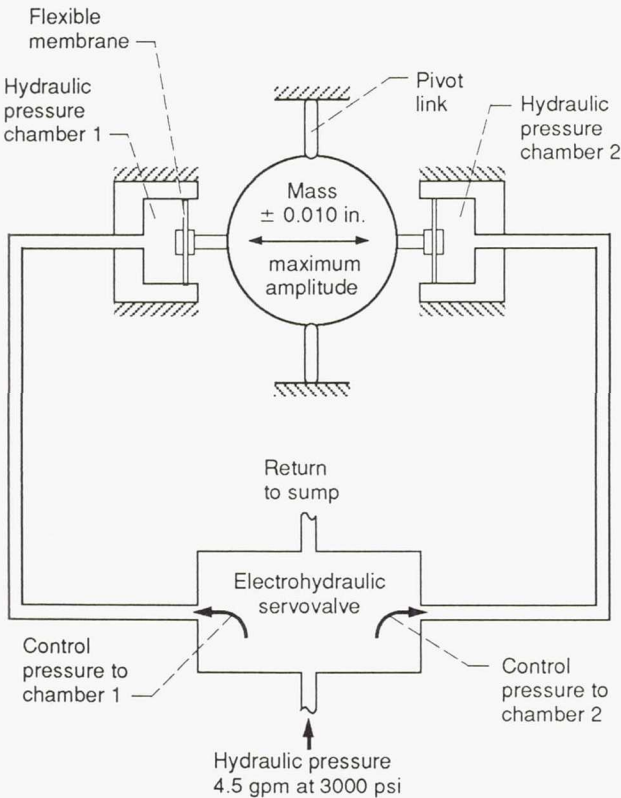


Figure 20.—Schematic of actively controlled hydraulic force actuator.

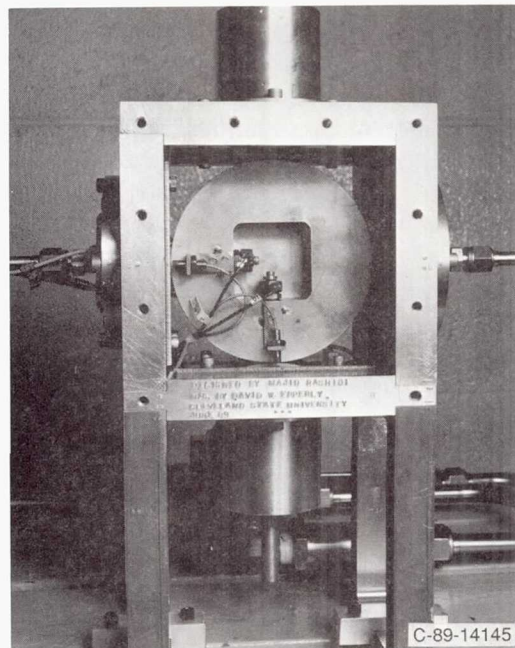


Figure 21.—Hydraulic force actuator rig.

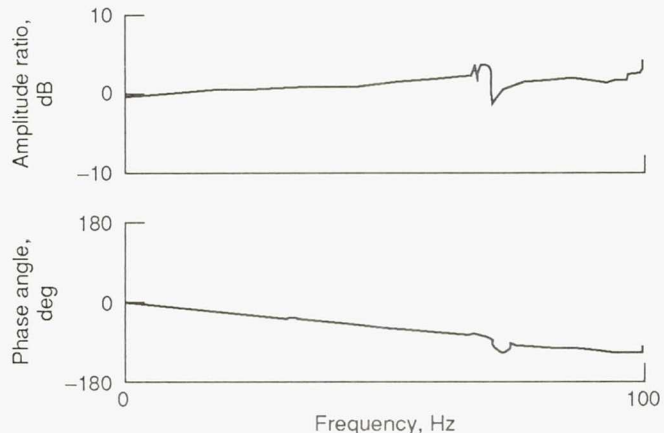


Figure 22.—Frequency response and phase shift.  
Mass amplitude, 0.0025.

due to the mass suspension and can be altered by changing the spring rate of the membranes or the weight of the mass. The focus of this work is to significantly increase the frequency response of the system so that it may be used to control rotor vibrations in typical advanced aircraft engines.

**Researchers:** H. Ulbrich (Technical University of Braunschweig), M. Rashidi (Cleveland State University), and E. DiRusso (NASA Lewis).

# Verification of Cryogenic Dampers

Cryogenic turbomachinery of the type used in liquid rocket high pressure fuel and oxidizer turbopumps have experienced high vibrations. Subsynchronous whirl instabilities, high unbalance sensitivities, and cross talk between the turbopumps are some causes for these high vibrations. These problems arise because of lack of damping in the pump. The damping contributed by seals may in some cases be inadequate or severely diminish as clearances increase with wear.

This research and development project proposes to develop generic sources of damping by designing and testing various types of dampers in a cryogenic environment. These dampers will alleviate the problem of insufficient damping in cryogenic turbomachinery.

Major goals are to (1) design, fabricate, and test a rotordynamics rig including a liquid nitrogen containment vessel for immersion of the dampers; (2) evaluate curved beam, elastomeric, active piezoelectric pusher, turbulent squeeze film, cartridge, non-Newtonian fluid, and other damper prototypes; and (3) design and test dampers for the Cryogenic Turbomachinery Test Stand at the NASA Lewis Research Center or the Marshall Space Flight Center.

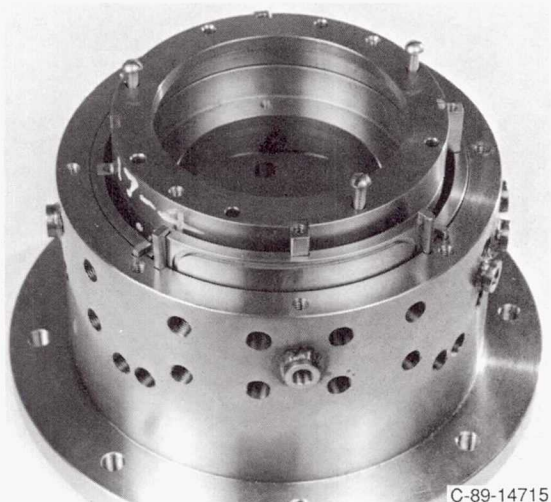


Figure 23.—Curved beam damper for cryogenic fluid.

20

A general purpose, rotordynamic test rig that uses liquid nitrogen as a working fluid was developed. The damper containment vessel (figs. 23 and 24) in this rig has a diameter of 24 in. and depth of 18 in. The installation of the rig is nearing completion, and testing of the curved beam damper (see figs. 23 and 24) will begin soon.

The rig is currently undergoing final machining for alignment and plumbing hookups. Damping measurements will be based on curve-fitting identification with a finite element model. Dynamic pressure will be measured in each curved beam to compare with theory and to verify the effectiveness of their O-ring seals. Future work includes

(1) Measuring the damping contributed by the curved-beam damper for various speeds, clearances, orifice sizes, outlet sharpness, supply pressures, and beam thickness and lengths

(2) Testing a cryogenic, piezoelectric active damper

(3) Testing a turbulent squeeze film damper that is similar to a standard squeeze film damper with turbulent circumferential flow

(4) Testing a cartridge type damper that will be sealed and will rely on shearing a remotely located, heated viscous fluid

(5) Installing a bearing below the damper in the damper containment vessel to allow the rotor bearing system to vary

(6) Adding a digital tracking filter for plotting synchronous response and identifying damping levels

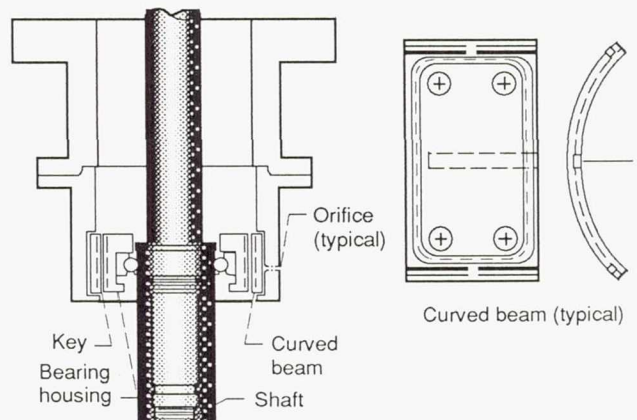


Figure 24.—Curved beam damper assembly.

**Researchers:** A.F. Kascak (AVSCOM) and A.D. Palazzolo, N. Olan, S.S. Ibrahim, and S. Jaganathan (Texas A&M).

# Hybrid Magnetic Bearing for Cryogenic Applications

A new magnetic bearing employing permanent magnets and electromagnets has been designed and fabricated by Avcon Incorporated under contract to NASA Lewis Research Center (Structural Dynamics Branch). This bearing is called a "hybrid magnetic bearing with permanent magnet bias" because it uses both permanent magnets and electromagnets. This bearing is smaller, lighter, and uses less electrical power than magnetic bearings currently used in industrial applications. These features make this bearing very attractive for aerospace applications. The bearing was designed for cryogenic applications for possible use in future space shuttle main engine turbopumps.

Conventional magnetic bearings (fig. 25) employ solely electromagnets to achieve suspension and control of rotors. Designs using only electromagnets require large amounts of electrical power at all times to suspend the rotor and to produce a bias magnetic flux. The bias magnetic flux linearizes the force-to-current relationship of the bearing, simplifying the bearing control system. In the hybrid magnetic bearing (fig. 26), the permanent magnets provide the bias magnetic flux, hence, electrical power is not required to perform this function. This means that the electromagnets use only a small amount of electrical power to keep the rotor centered in the

presence of random disturbances and to counter any high dynamic forces on the rotor. Therefore, the hybrid bearing has a very large savings of electrical power over conventional magnetic bearings.

In previous permanent magnet bias bearings, the electromagnet flux had to pass through the permanent magnets, resulting in inefficient use of the electromagnet flux. In this new concept, the permanent magnets are not in the electromagnet flux path, so the efficiency of the electromagnets is not compromised. This is accomplished by arranging the permanent magnets so that they produce flux lines along the axis of the rotor while the electromagnet flux lines are circumferential (fig. 26).

The hybrid magnetic bearing designed under this contract has a radial load capacity of 500 lb. Figure 27 shows the component parts. The bearing has an air gap diameter of 3.0 in., a stator outside diameter of 5.25 in., and a length of 4.12 in. The bearing was installed into an existing Lewis rig capable of operating up to 15 000 rpm. This speed is limited by the rig, not the magnetic bearing.

Preliminary tests of the bearing have been performed at room temperature for radial loads up to 400 lb, stiffness up to 100 000 lb/in., and speeds

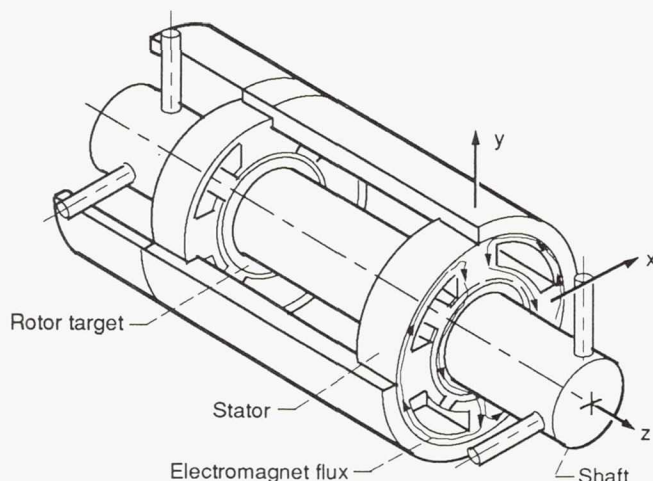


Figure 25.—Conventional all-electromagnet magnetic bearing.

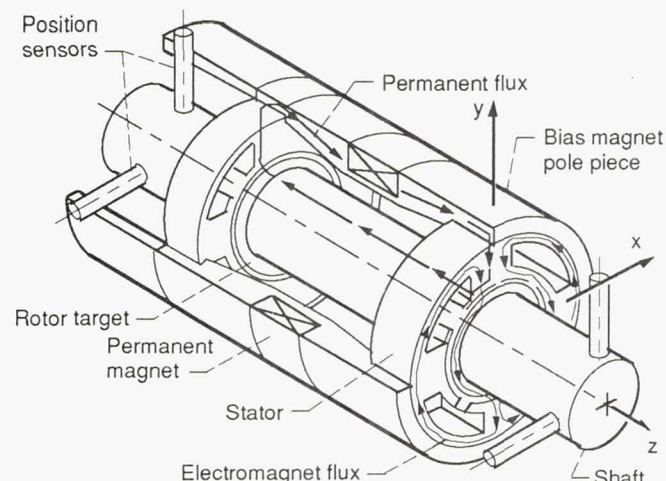


Figure 26.—Hybrid magnetic bearing with permanent magnet bias.

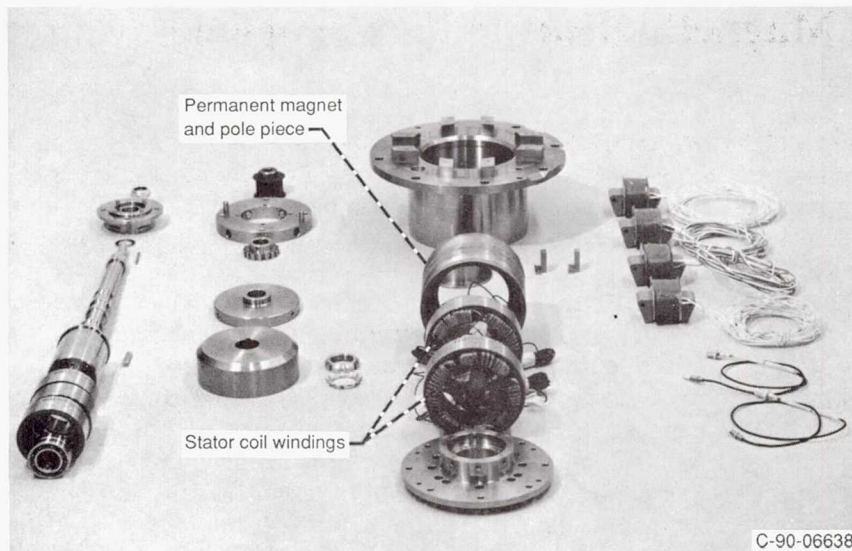


Figure 27.—Hybrid magnetic bearing component parts.

up to 2500 rpm. Figure 28 compares actuator power consumption (power in the electromagnetic coils) for the hybrid magnetic bearing with a conventional all-electromagnet design at room temperature. The figure indicates that the hybrid bearing power consumption at zero radial load is 1/100 of

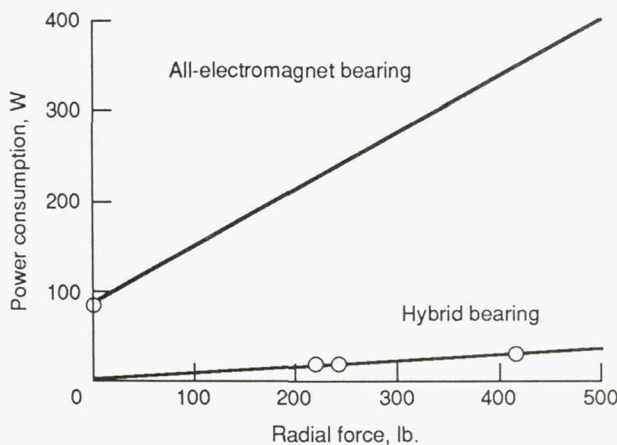


Figure 28.—Actuator power consumption.

the power consumption of a conventional magnetic bearing and 1/10 at 500-lb radial load. Measurements of total power consumption, including the servoelectronics and power supplies, show 15 W required for static levitation and 32 W for a steady radial load of 40 lb at 2000 rpm. It is anticipated that the radial force capability of the bearing can be doubled without increasing the physical size of the bearing with only minor changes in the servo-electronics. The power supply and servocontrol electronics are housed in a rectangular box 17 by 14 by 8.5 in., for the prototype bearing, but they can be packaged in a much smaller volume. This is a very significant reduction in the size and weight of the servo and power-supply electronics.

Lewis Research Center plans further testing of this bearing at liquid nitrogen temperature (-321 °F) and speeds up to 15 000 rpm.

---

**Researchers:** E. Dirusso and G.V. Brown (NASA Lewis), A.F. Kascak (AVSCOM), and D.P. Fleming (NASA Lewis).

# Active Vibration Control (AVC) Test Results

Active vibration control (AVC) tests on the Lewis high-speed balance rig were conducted during the summer of 1989. Figure 29 shows that opposing pushers were installed at both bearings, whereas only nonopposing pushers were installed at the outboard disk in the summer 1988 tests. Tests showed that the opposing pushers provided significantly more active damping than a single pusher and that they also prevented misalignment due to the unidirectional preload of the nonopposing pusher configuration. Figure 29 also shows two overhung disks instead of the single outboard disk used in the summer 1988 tests. The additional inboard disk provided a means to vibrate both ends of the shaft. The unbalanced response test confirmed that vibrations could be effectively suppressed along the entire shaft assembly with the sensor/actuator configuration in figure 29. A room temperature elastomeric pad was used to isolate the piezoelectric actuators from the rig's housing and bearing retainer in the summer 1988 test. A high-temperature (full damping capability at 300 °F) elastomeric pad was used in the summer 1989 test. This pad was required to isolate the piezopusher only from the rig's housing in the summer 1989 test. This and the increased stiffness of the high temperature pad provided additional

active damping and yielded an actuator system that could respond effectively at higher frequencies. The active damper control capability increased from 6500 rpm (1988 testings) to over 13 000 rpm (1989 test).

Figure 30 shows the analog control circuit utilized in the summer 1989 test. This circuit provides any combination of proportional (active stiffness) and derivative (active damping) feedback. The summing and buckout circuits were utilized to account for the "off-axis" probe configuration and to remove the dc bias voltage. Static stiffness, maximum stroke, and displacement sensitivity tests were conducted on each of the eight pzl-100 Burleigh piezoelectric pushers, yielding the following results:

Static stiffness, lb/in. ....	17 000 to 29 000
Maximum stroke <sup>a</sup> , mils (p-p). ....	3.2 to 5.2
Sensitivity <sup>a</sup> , V/mil. ....	1.30 to 1.40

<sup>a</sup>Evaluated with a Sine wave input to the driver at a frequency of 200.0 Hz and a voltage of 1.0 V (p-p).

Transfer functions were also made for each piezoelectric pusher and its respective driver.

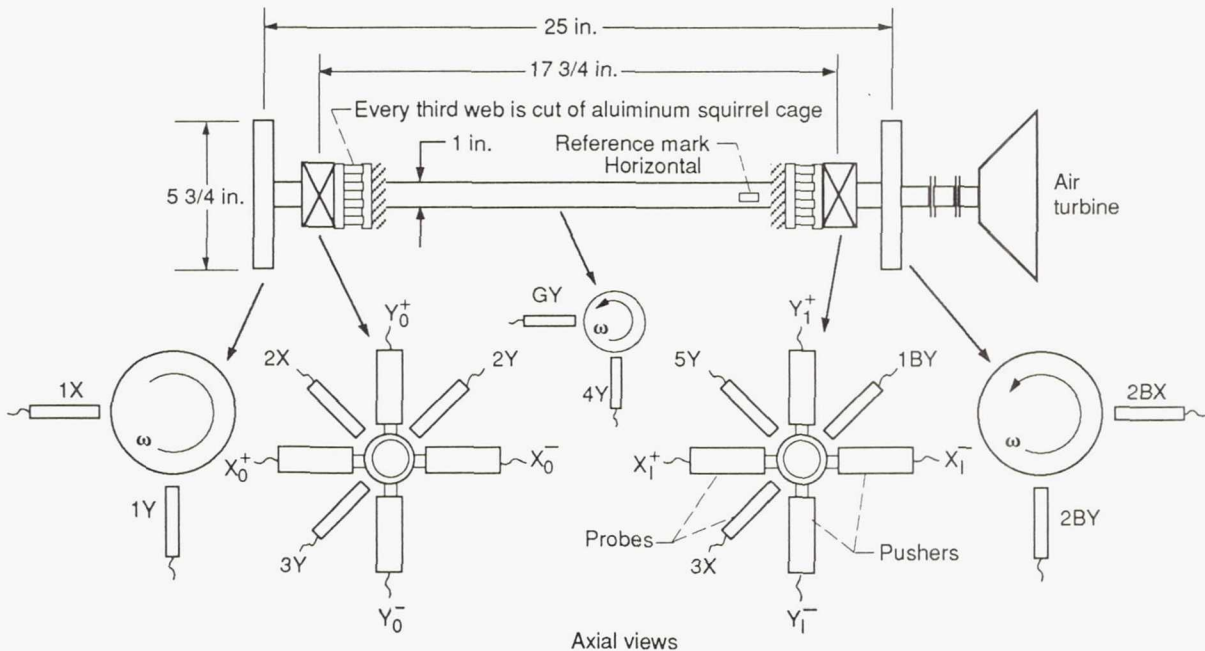


Figure 29.—Machinery, transducer, and sensor arrangement.

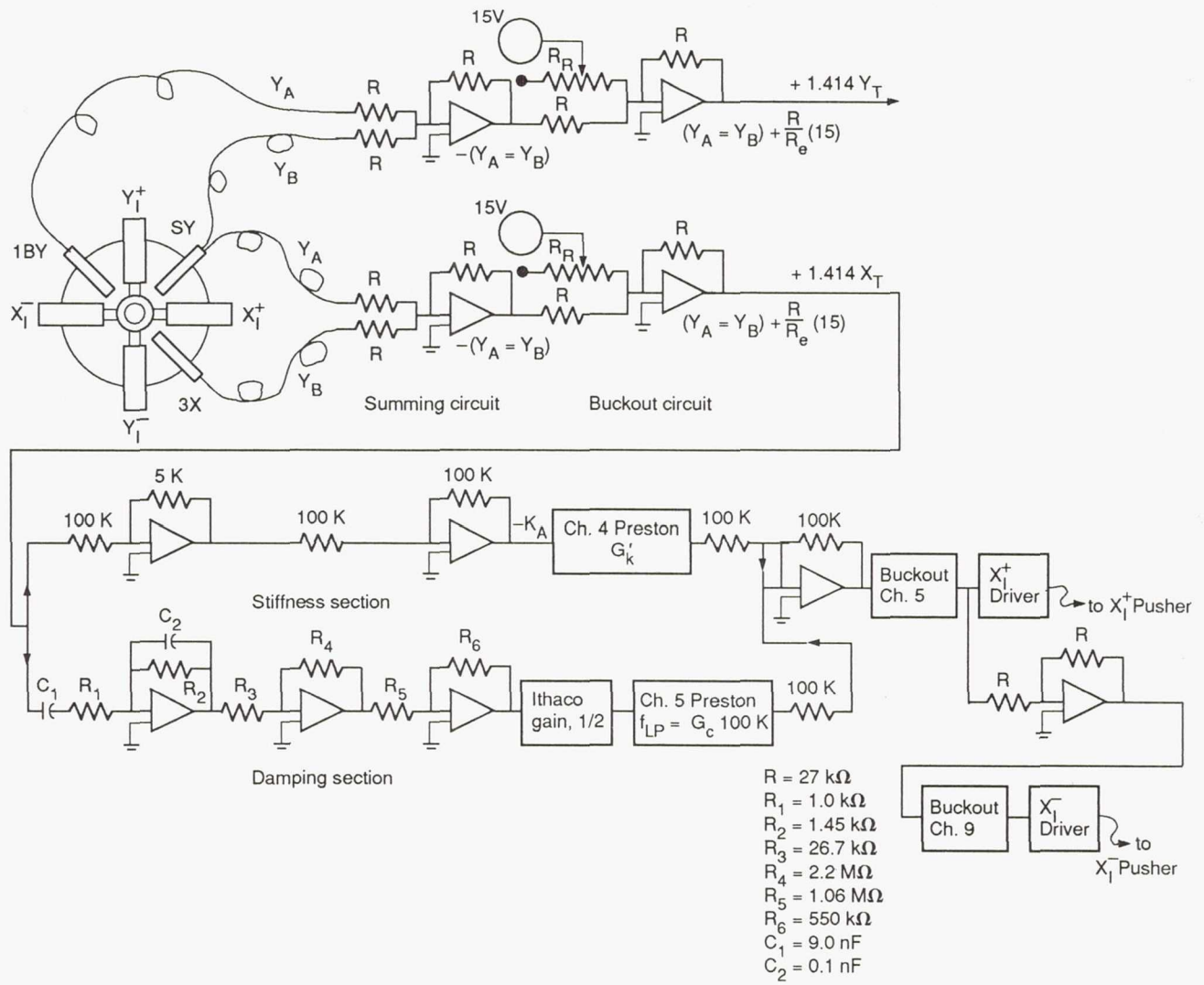


Figure 30.—Control circuit diagram.  $Y_T$  and  $X_T$  are averaged  $Y$  and  $X$ , respectively;  $G_k$  is gain for stiffness feedback;  $G_c$  is gain for damping feedback.

Figure 31 shows the effect of active damping in suppressing the second mode unbalance response at 13 000 rpm. The data in this figure were measured at the outboard bearing housing. Figure 32 shows data measured at the midspan of the rotor. The first mode response at 10 100 rpm was suppressed with active stiffness, while the second mode response was suppressed by a combination of active stiffness and damping.

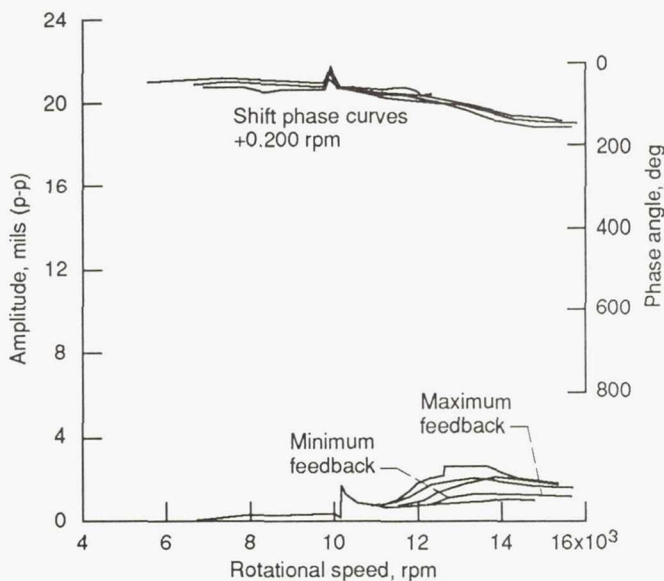


Figure 31.—Outboard bearing vibration versus active damping gain,  $G'_c$ . Effect of active damping on second mode, 13 000 rpm.

“Sudden mass imbalance” tests were conducted to determine the effectiveness of the control systems for suppressing transient response. The results (Figure 33) showed significant vibration reduction even at 12 000 rpm, which was much higher than the corresponding speed (6500 rpm) in the 1988 testing.

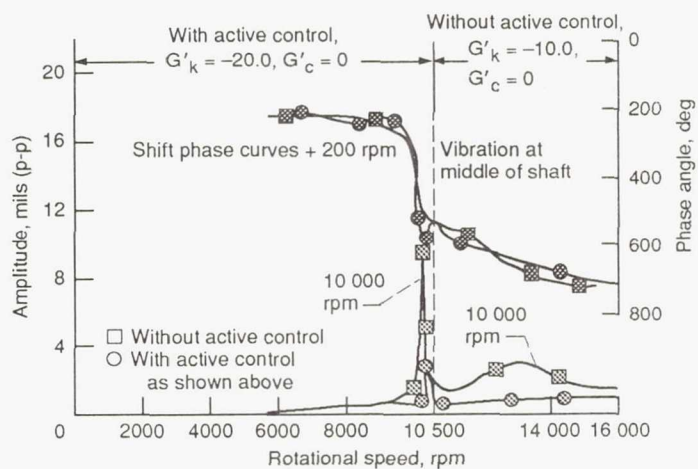


Figure 32.—Midspan vibration with and without active damping and stiffness. Effect of active stiffness and active damping on first and second mode.

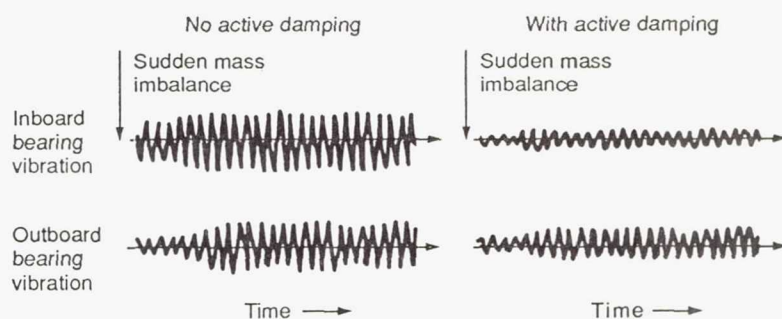


Figure 33.—Shaft turning at 12 000 rpm. Sudden mass imbalance 0.35g at 2.5 in. from the outboard end.

---

**Researchers:** A.F. Kascak (AVSCOM), G.T. Montague (Sverdrup), and A.D. Palazzolo, R.R. Lin, S. Jaganathan, and D. Roever (Texas A&M).

## Active Vibration Control Theory

Electromechanical instability is a limiting factor in achieving higher levels of active damping. This phenomena results from the nonideal behavior of any sensor or actuator, and is characterized by increasing phase lag with frequency. The achievable level of active damping (while maintaining stable operation) can be raised by structural or electrical means. Phase lead and filtering circuits may help by decreasing phase lag or eliminating certain bands of the feedback spectrum. However, these devices also have detrimental effects including low-frequency amplitude attenuation and phase lag. Consideration of these factors convinced the principal investigator that the optimum implementation of the piezoelectric actuator—active vibration control (AVC) will involve simultaneous design of the electrical control system and the structural rotor-bearing system. This

design tool, which is under development at Texas A&M, consists of software to predict the instability onset gain level. The capability of this software will be tested by comparing its output with results obtained on the Lewis transient dynamics rig in the summer 1989. The Lewis rig became unstable at approximately 2100 Hz. The corresponding mode shape was identified from transient recorder plots (fig. 34) and is shown in figure 35.

Figure 36 shows a sketch for an isolated bearing in an active damping type vibration control. The opposing piezoelectric actuators are soft-mounted on flexible springs (elastomer). Figure 37 shows the equivalent electromechanical model of this setup. Both the piezoelectric pusher and its driver are represented as second-order, electrical, low-pass

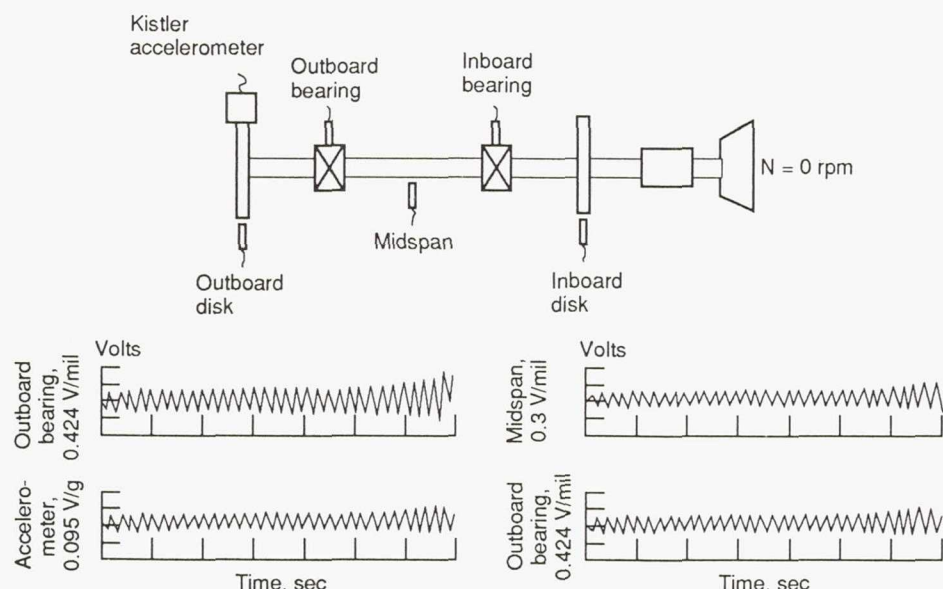


Figure 34.—Transient data records for unstable mode determination. All  $\gamma$  probes and accelerometers; all ITHACO's cut off at 5000 Hz; only  $Y_0^+$  and  $Y_0^-$  pushers operating; however, all others are installed; feedback gain,  $G'_c$ , 4.6, and  $G'_k$ , 0.0.

filters. This representation was formulated on the basis of measured transfer functions of the pusher and its driver.

Areas for future work include

- (1) Development of software to predict instability onset gains for rotor bearing systems, including an AVC system with nonideal actuators and sensors
- (2) Development of a digital filter to remove the high-frequency phase lag of actuators and sensors without introducing any additional phase lag of its own

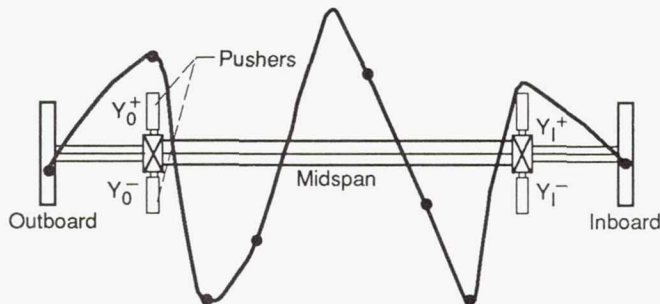


Figure 35.—Unsteady mode shape. Frequency, 2100 Hz.

(3) Development of a digital control system that will utilize the excitation capability of the actuator to detect significant changes in the rotor natural frequencies (This is a good indicator of structural flaws, as part of a maintenance program.)

(4) Development of a digital control system that will measure modal characteristics with the piezoelectric actuators and will use this to develop a control strategy.

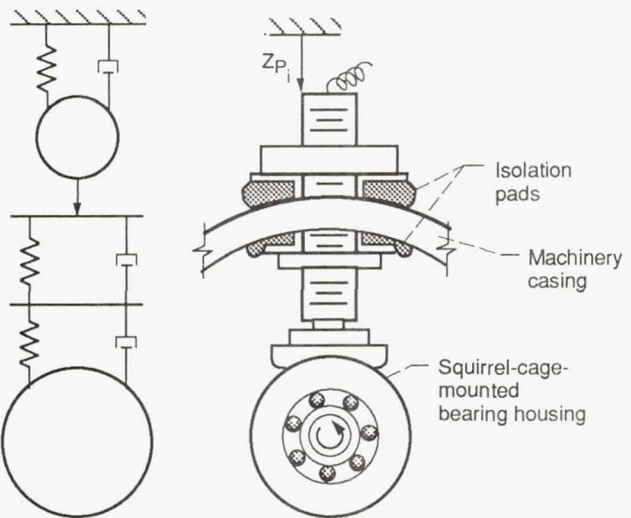


Figure 36.—Idealized representation of the pusher and its connections.

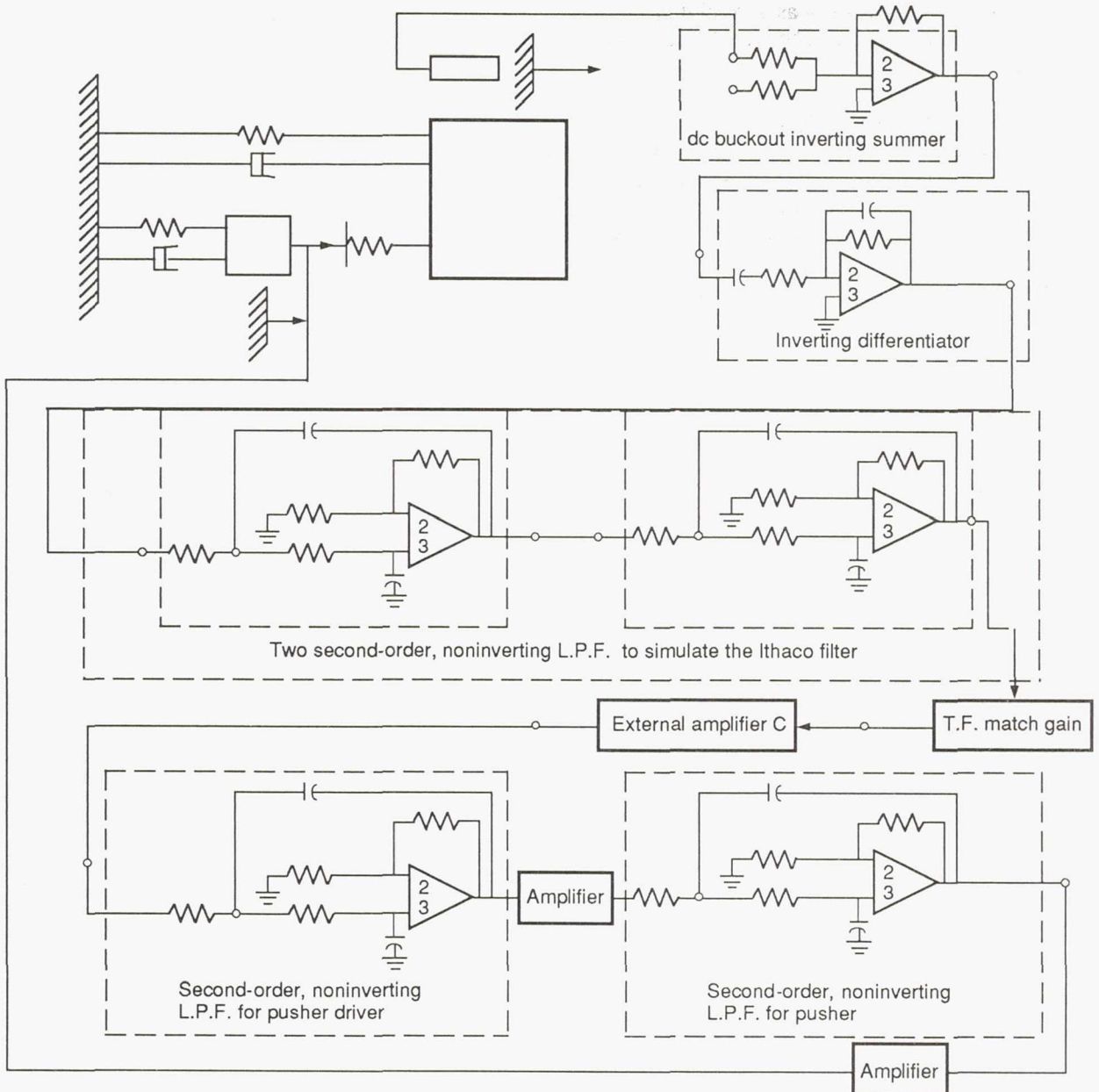


Figure 37.—Single pusher with absorber.

**Researchers:** A.F. Kascak (AVSCOM), G.T. Montague (Sverdrup), A.D. Palazzolo, R.R. Lin, S.Jaganathan, D. Roever, and T. Barrett (Texas A&M).

# A Global Approach for the Identification of Structural Connection Properties

A general procedure was developed to identify properties of structural joints. The procedure, which uses experimental response data, is considered general because it can be applied to any size or type of structural system. Furthermore, characteristics such as damping and stiffness, as well as nonlinearities in joints, may be identified.

Since joints usually contribute significantly to the overall system stiffness, damping, and in many cases nonlinearity, it is critical that reliable joint models be made available. For many structural systems the constituent components often may be modeled accurately, but the joints contain considerable modeling uncertainty. Therefore, accurate system response predictions often are highly dependent on valid joint models.

The present procedure is applicable to both linear and nonlinear joints and is suitable for processing test data that have been measured at arbitrary stations on the structural system. The method identifies joint parameters by performing a "global" fit between the predicted and measured data. The method is advantageous over previous methods because it can better deal with parameter-dependent constraints (e.g., gaps).

The method was demonstrated (fig. 38) with a bladed-disk assembly with friction damping. This assembly was used for the demonstration because it is a relatively complex system and exhibits considerable joint damping. For typical bladed-disk assemblies, the dominant joint damping originates from blade tip rubbing or from interblade friction forces acting at the blade's shroud locations.

The complete structural system was excited at various stations along the structure, and the resulting response (e.g., displacements and velocities) was measured to identify the connection parameters. The measurement stations may, or may not, be collocated with the excitation, and the number of measurement stations may, or may not, be equal to the number of input excitations. In general, it was simpler to excite the system with a single input, and then measure the resulting response at multiple stations. It is required that both the input be known and the output be measured, regardless of the number of stations. The response measurements

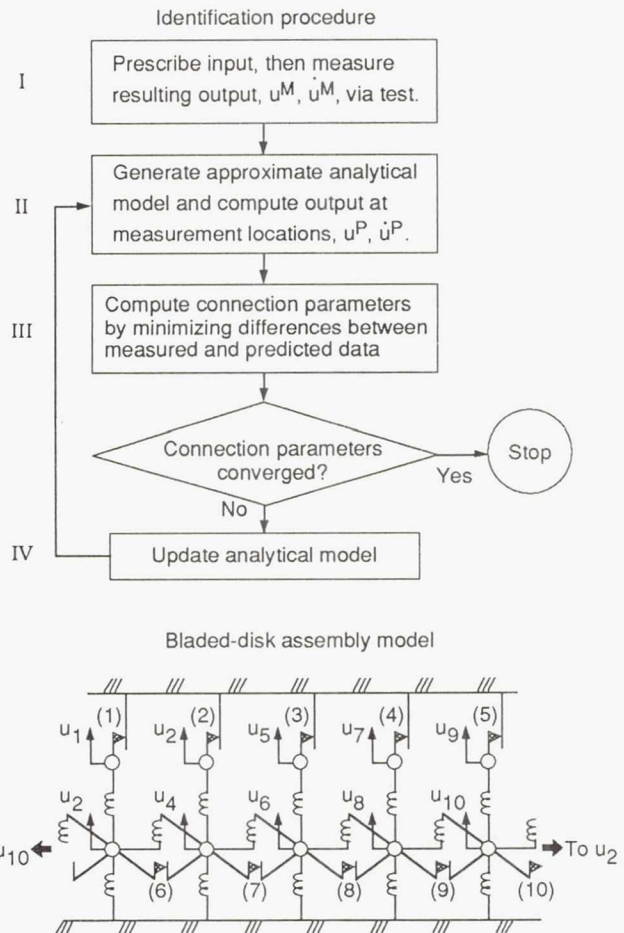


Figure 38.—Identification of connection properties. Parentheses () indicates parameter: 1 to 5 tip, 6 to 10 midchord;  $u$  indicates degree of freedom.

need not be stationed directly at the connection boundaries, but instead may be established at any convenient position on the system.

The transient response (fig. 39) was obtained by exciting the system with a nonuniform initial displacement. In the first iteration where the predictor model does not yet have any damping, there is very little agreement between the predicted and actual response. As expected, the experimental response decays quite rapidly because of the damping in the experimental model, while the predicted response does not decline at all. By the sixth iteration, there is general agreement between the predicted and experimental data, and after thirty-five iterations there is no noticeable difference between the two responses.

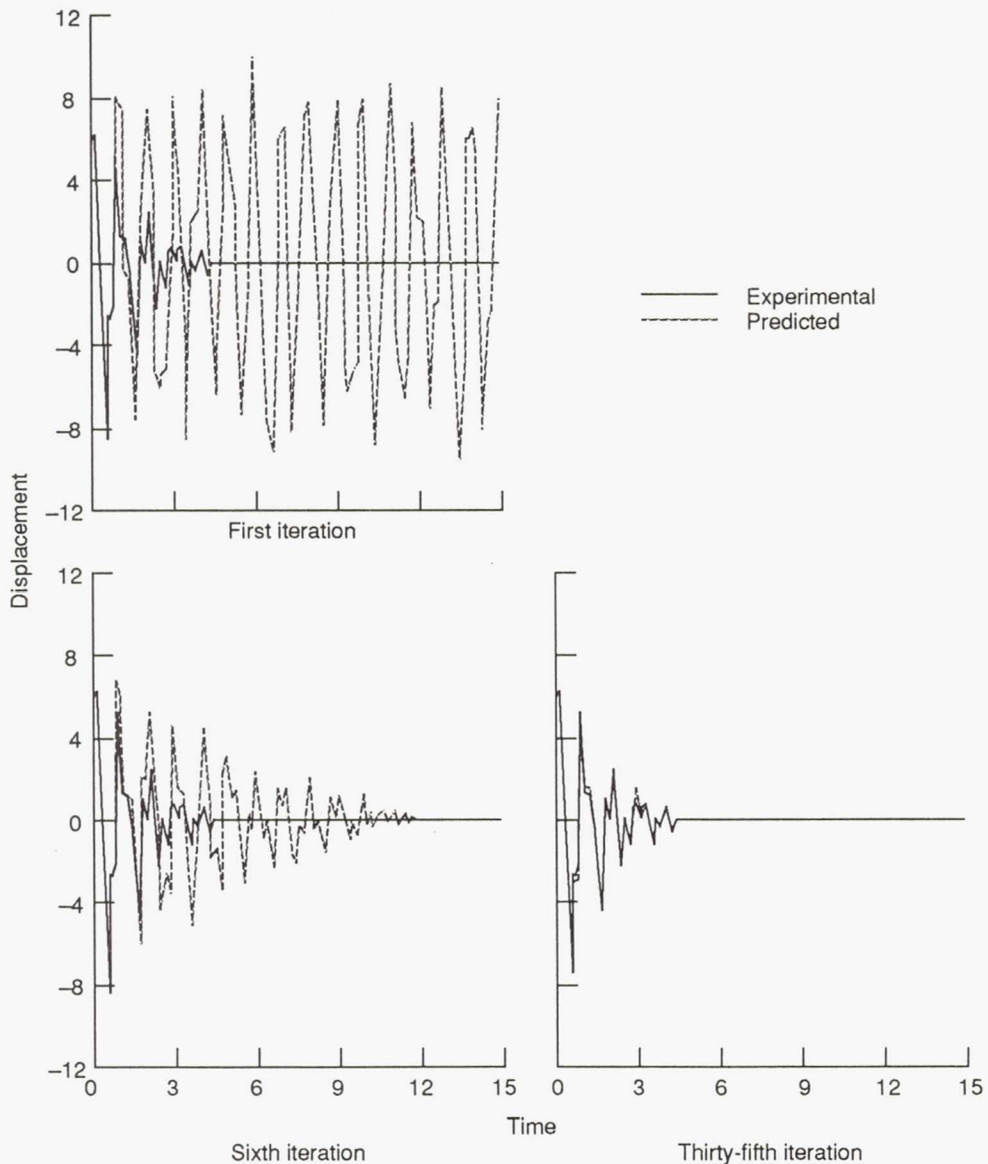


Figure 39.—Comparison between experimental and predicted transient response (512 time steps).

Overall, there is very reasonable agreement between the actual and identified parameters for different levels of measurement error and mistuning. In general, the quality of the parameter identification depends on the quantity as well as the quality of the system transient response data available. The number of parameters to be identified is not limited, although larger identification problems may require a greater number of measurement stations. Although larger problems will require greater CPU (central

processing unit) usage, the usage should not become prohibitively large except for applications requiring real- or fast-time identification, such as may be necessary for real-time control. The procedure shows great promise for improving modeling capabilities in complex structural systems, as well as for enhancing our understanding of structural behavior.

---

**Researchers:** C. Lawrence (NASA Lewis) and A.A. Huckelbridge (Case Western Reserve).

# Contact Area Temperature Profile of an Engaging Sprag Clutch

The sprag overrunning clutch is an integral part of a helicopter's drivetrain. It transmits torque from the engine to the combining gearbox and overruns when the gearbox output rotates faster than the engine. These clutches operate on the wedging action of small sprags located between the inner and outer race. The kinematics of an engaging sprag are understood; however, what is occurring at the sprag inner-race contact area has not yet been studied. During lockup, the sprag rotates and produces high pressures and temperatures due to the squeezing of the oil film. Figure 40 represents the theoretical temperature profile that is generated at the contact point. A four-square test rig has been constructed to determine the magnitudes of these temperatures since they may approach the tempering range of the inner race material. Data from this test will then help validate a finite element computer code that models the engagement process of the clutch.

Figure 41 shows the layout of the four-square test rig. Power is supplied by a 200-hp variable-speed dc electric motor and is transferred to the system

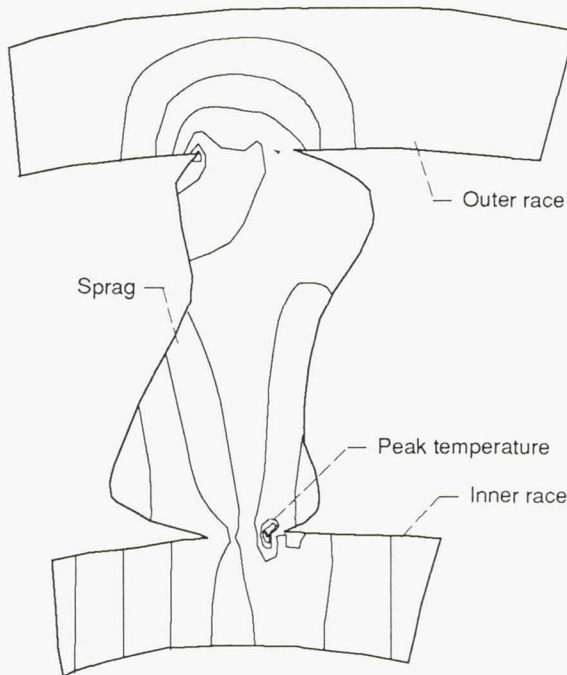


Figure 40.—Temperature profile of sprag.

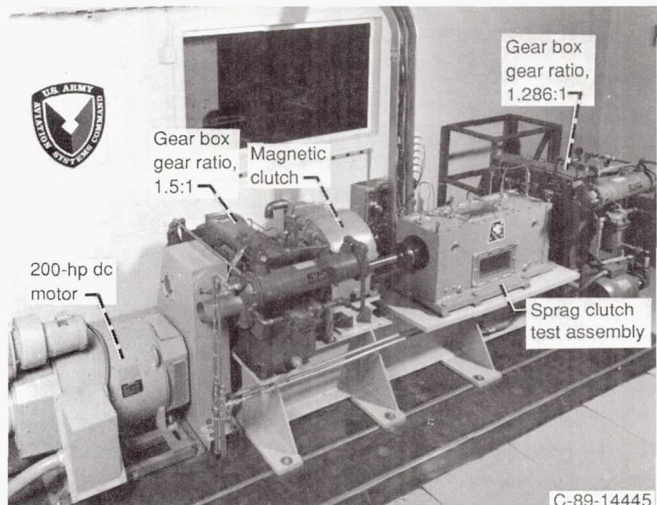


Figure 41.—Sprag clutch engagement test rig.

through a pulley and belt arrangement. The closed-loop is configured with two end gearboxes with ratios of 1.50° and 1.286, which allow a difference in rotating speeds between the input and output shafts of the magnetic clutch. The sprag clutch test assembly is located on the high-speed shaft with the outside race of the clutch driving the inside race. The inner race has been instrumented with eight thermocouples positioned to give the greatest probability of being near an engaging sprag.

The tests will be run with the clutch test assembly rotating at 5000 rpm. During the operation of the rig, the sprag clutch will be initially engaged because of the inertia of the shafts and gears. Full sprag lockup will occur when a voltage is manually applied across the magnetic clutch, increasing the torque and decreasing the speed of the sprag clutch's output shaft. At that time, temperature measurements will be taken. This will be repeated for a number of engagement cycles since it is difficult to determine when a sprag is directly over a thermocouple. The highest readings from all the cycles performed will be taken as true sprag engagement temperatures.

---

**Researchers:** K.C. Radil and A.F. Kascak  
(AVSCOM).

## **Dynamic Substructuring by the Boundary Flexibility Vector Method of Component Mode Synthesis**

Component mode synthesis (CMS) is a method of dynamic analysis, for structures with a large number of degrees of freedom (DOF). These structures often require lengthy computer CPU (central processing unit) time and large computer memory resources, if solved directly by the finite-element method. In CMS, the structure is divided into independent components in which the DOF are defined by a set of generalized coordinates defined by displacement shapes. The number of the generalized coordinates are much less than the original number of physical DOF in the component. The displacement shapes are used to transform the component property matrices and any applied external loads to a reduced system of coordinates. Reduced system property matrices are assembled, and any type of dynamic analysis is carried out in the reduced coordinate system. Final results are back-transformed to the original component coordinate systems. In all conventional methods of CMS, the mode shapes used for components are dynamic mode shapes, supplemented by static deflected shapes. Historically, all the dynamic mode shapes used in conventional CMS are the natural modes (eigenvectors) of components.

In this work a new method of CMS, namely the boundary flexibility vector method of CMS, is developed. The method utilizes a set of static Ritz vectors, referred to as boundary flexibility vectors, as a replacement and/or supplement to conventional eigenvectors and as displacement shapes for characterizing components. The generation of these vectors does not require the solution of a costly eigenvalue problem, as in the case of natural modes in conventional CMS, and hence a substantial saving in CPU time can be achieved. The boundary flexibility vectors are generated from flexibility (or stiffness) properties of components. The formulation presented is for both free- and fixed-interface components, and for both the free and forced vibration problems. Free and forced vibration numerical examples are presented to verify the accuracy of the method and the savings in CPU time.

Compared with conventional methods of CMS, the results indicate that, by using this new method, more accurate results can be obtained with a substantial savings in CPU time. A comparison of the number of operations required to obtain the boundary flexibility vectors versus normal modes of vibration, showed a substantial reduction of the number of required operations when boundary flexibility vectors were used instead of eigenvectors. Good agreement with finite-element and conventional methods of CMS was found after the new method was applied to a substantially large structure. An average savings of CPU time between 75 and 80 percent was attained. The results obtained by the boundary flexibility method of CMS, also were in good agreement with the results obtained from the direct integration of the equations of motion. In all cases considered, the results obtained by the boundary flexibility method were almost the same and sometimes superior to those obtained by conventional methods of CMS.

---

**Researchers:** A.A. Abdallah and  
A.A. Hucklebridge (Case Western Reserve) and  
C. Lawrence (NASA Lewis).

## MIMD (Multi-Input, Multidata) Parallel FORTRAN Configuration File Generator

Implementing a parallel application on a message-passing architecture involves a two-part mapping: the software tasks must be mapped to the distribution processing nodes, and the communications between tasks must be mapped to communications paths in the parallel architecture. After the software tasks are mapped to the nodes, the Configuration File Generator (CFG) completes the implementation by automatically generating a suitable mapping for the software channels.

This utility maps a parallel FORTRAN application to a transputer system. "Multiplexor/demultiplexor" tasks are provided everywhere that multiple software channels are mapped to a single hardware channel. For communication between two tasks residing on nodes that are not connected by a physical link, a communications path is established. This path consists of a sequence of "intermediate" tasks on nodes between the two nodes. The duty of each intermediate node is to receive messages on the single input channel and send them out on the output channel.

### Input:

- (1) A set of FORTRAN programs, each representing a task
- (2) A partial configuration file giving the hardware declarations, task declarations, and assignment of software tasks to physical processors

### Output:

- (1) A complete configuration file (fconfig.cfg)
- (2) Any utility tasks (multiplexor, demultiplexor, and intermediate) expressed as FORTRAN programs as needed

The mapping of software channels to hardware channels is a complex task and is prone to errors when left to the programmer. Not only does CFG ensure an error-free mapping, it facilitates frequency reconfiguration during development and testing.

---

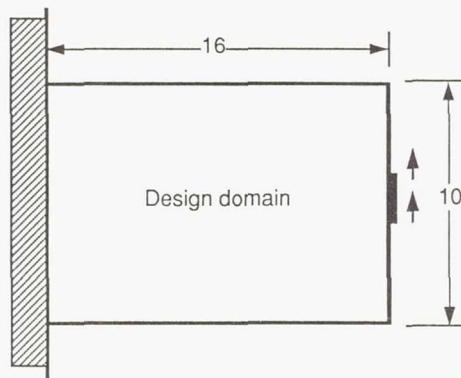
**Researchers:** H. Standley (University of Toledo) and L.J. Kiraly (NASA Lewis).

## Shape and Topology Optimization by the Homogenization Method (Verification Studies)

A major difficulty in optimizing the shape of linearly elastic structures is caused by large domain changes during the optimization process. Because of these changes, the domain must be rediscritized for the finite element stress analysis. Furthermore, changes of topology, such as the introduction of weight-saving holes in the structure, are virtually impossible to optimize with existing approaches, unless they are done manually. To resolve these difficulties and limitations of traditional shape optimization, a new method was developed. In a fixed domain subject to given load and support conditions, shape and topology are optimized and discretized automatically with a "unit cell" approach. The design domain is discretized into a gridwork

pattern of unit cells whose areas are modified sequentially until the compliance of the structure is minimized subject to a user-defined allowable structural weight (i.e., area  $\times$  thickness  $\times$  density). During the optimization, the unit cell areas are tailored with a percent-void parameter that varies between 0.0 for a heavily loaded (e.g., full) unit cell to 1.0 for a lightly loaded (e.g., empty) cell.

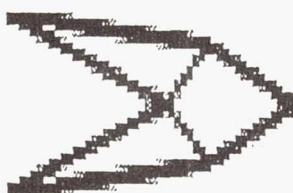
The goals of the current work were to examine the convergence of the code and to numerically verify that the final structural shapes predicted were those predicted by classical methods. The first study examined whether the final shape arrived at by the code was unique and independent of the



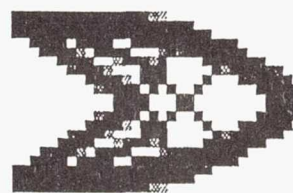
(a) Cantilever subjected to vertical force at free end.



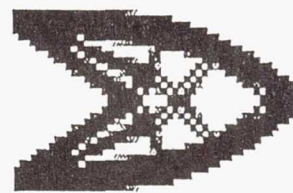
32 by 20 mesh



48 by 30 mesh



32 by 20 mesh



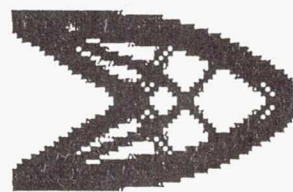
48 by 30 mesh



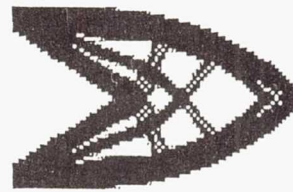
64 by 40 mesh



80 by 50 mesh



64 by 40 mesh

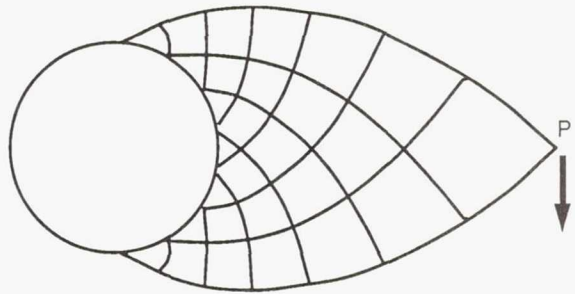


80 by 50 mesh

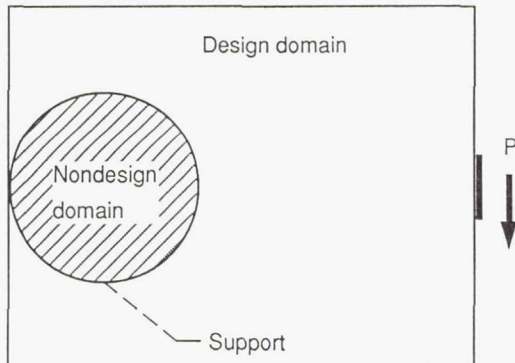
(b) Resulting structure with 40 percent of initial weight.

(c) Resulting structure with 80 percent of initial weight.

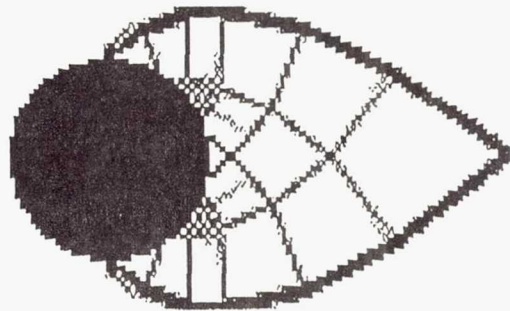
Figure 42.—Comparison of resulting structure for four increasingly refined meshes and two user-specified final weights.



(a) Analytical solution of Michell truss with vertical load,  $P$ , at free end.



(b) Initial model. Domain discretized with unit cell elements.



(c) Resulting optimized structure.

Figure 43.—Comparison of optimized structure predicted by unit cell approach to classical Michell truss.

initial unit-cell mesh. To check this convergence a short cantilever rigidly attached to a wall at its left end was subjected to a vertical force at its free end (fig. 42(a)). The initial design domain was discretized with four unit-cell meshes of increasing refinement, (e.g., 32 by 20, 48 by 30, 64 by 40, and 80 by 50 equal-sized finite elements).

The results of this study for two user-defined final weights corresponding to 40 and 80 percent of the initial weight are shown in the lower half of figure 42. It is clear from these results that the final shapes predicted for each weight budget converge and that the predicted overall shape is relatively insensitive to the initial unit-cell mesh. Another feature observed from this study is that the shape and topology can be predicted with a relatively crude mesh. This feature is important to structural engineers wanting a quick but accurate preliminary design of a machine component.

Another key study was to determine if the current unit cell approach predicted structures expected from

classical theory. The Michell Truss shown in figure 43(a) is known as the optimal truss structure for carrying bending loads to a circular attachment point. This problem is modeled in figure 43(b) with the left end of the design domain supported by a circular peg and the right end loaded with an over-hung load  $P$ . The structural shape predicted by the homogenization method is shown in figure 43(c) and bears a remarkable resemblance to the Michell Truss. It is clear that the present methods predict the characteristic trusslike frames that are mutually orthonormal in most of the domain. Some small differences are observed at the circular boundary because of the rigid connections used in this analysis instead of the hinge connections generally assumed in the analytical study of the Michell Truss.

---

**Researchers:** N. Kikuchi and K. Suzuki  
(University of Michigan) and B. Steinmetz (NASA Lewis).

## Appendix—Researchers

Abdallah, A.A.	Analex Corporation, Fairview Park, Ohio
Bakhle, M.A.	The University of Toledo, Resident Research Associate at NASA Lewis Research Center, Cleveland, Ohio
Barrett, T.	Texas A&M University, College Station, Texas
Bliss, D.B.	Duke University, Durham, North Carolina
Brown, G.V.	NASA Lewis Research Center, Cleveland, Ohio
DiRusso, E.	NASA Lewis Research Center, Cleveland, Ohio
Dowell, E.H.	Duke University, Durham, North Carolina
Fleming, D.P.	NASA Lewis Research Center, Cleveland, Ohio
Hall, K.	United Technologies Research Center, E. Hartford, Connecticut
Huckelbridge, A.A.	Case Western Reserve University, Cleveland, Ohio
Huff, D.L.	NASA Lewis Research Center, Cleveland, Ohio
Ibrahim, S.S.	Texas A&M University, College Station, Texas
Jaganathan, S.	Texas A&M University, College Station, Texas
Janetzke, D.C.	NASA Lewis Research Center, Cleveland, Ohio
Kascak, A.F.	U.S. Army Aviation Research and Technology Activity—AVSCOM, NASA Lewis Research Center, Cleveland, Ohio
Kaza, K.R.V.	NASA Lewis Research Center, Cleveland, Ohio
Keith, T.G.	The University of Toledo, Toledo, Ohio
Kikuchi, N.	University of Michigan, Ann Arbor, Michigan
Kiraly, L.J.	NASA Lewis Research Center, Cleveland, Ohio
Kurkov, A.P.	NASA Lewis Research Center, Cleveland, Ohio
Lakatos, T.F.	NASA Lewis Research Center, Cleveland, Ohio
Lawrence, C.	NASA Lewis Research Center, Cleveland, Ohio
Lin, R.R.	Texas A&M University, College Station, Texas
Lucero, J.M.	NASA Lewis Research Center, Cleveland, Ohio
Mahajan, A.J.	The University of Toledo, Toledo, Ohio
Mehmed, O.	NASA Lewis Research Center, Cleveland, Ohio
Montague, G.T.	Sverdrup Technology, Inc., Lewis Research Center Group, Brook Park, Ohio
Murthy, D.V.	The University of Toledo, Resident Research Associate at NASA Lewis Research Center, Cleveland, Ohio
Olan, N.	Texas A&M University, College Station, Texas
Palazzolo, A.D.	Texas A&M University, College Station, Texas
Radil, K.C.	U.S. Army Aviation Research and Technology Activity—AVSCOM, NASA Lewis Research Center, Cleveland, Ohio
Rashidi, M.	Cleveland State University, Cleveland, Ohio
Reddy, T.S.R.	The University of Toledo, Resident Research Associate at NASA Lewis Research Center, Cleveland, Ohio
Roever, D.	Texas A&M University, College Station, Texas
Sankar, N.L.	Georgia Institute of Technology, Atlanta, Georgia
Smith, T.E.	Sverdrup Technology, Inc., Lewis Research Center Group, Brook Park, Ohio
Srivastava, R.	Georgia Institute of Technology, Atlanta, Georgia
Standley, H.	The University of Toledo, Toledo, Ohio
Stefko, G.L.	NASA Lewis Research Center, Cleveland, Ohio
Steinetz, B.M.	NASA Lewis Research Center, Cleveland, Ohio
Suzuki, K.	University of Michigan, Ann Arbor, Michigan
Ulbrich, H.	Technical University of Braunschweig, Braunschweig, Federal Republic of Germany
Verdon, J.	United Technologies Research Center, E. Hartford, Connecticut
Williams, M.H.	Purdue University, West Lafayette, Indiana

## Bibliography

- Afolabi, D.: Effects of Mistuning and Matrix Structure on the Topology of Frequency Response Curves. NASA TM-102290, 1989.
- Bakhle, M.A.; Reddy, T.S.R.; and Keith T.G., Jr.: Time Domain Flutter Analysis of Cascades Using a Full-Potential Solver. 31st Structures, Structural Dynamics and Materials Conference, Part 3, AIAA, 1990, pp. 1489-1496.
- Bendiksen, O.O.; Boschitsch, A.H.; and Quackenbush, T.R.: New Computational Method for Aeroelastic Problems in Turbomachines. CDI Report No. 89-07, Continuum Dynamics, Inc., Princeton, N.J., NASA Contract NAS3-25574, Oct. 1989.
- DiRusso, E.; and Brown, G.V.: Experimental Evaluation of a Tuned Electromagnetic Damper for Vibration Control of Cryogenic Turbopump Rotors. NASA TP-3005, 1990.
- Dodd, W.R.; Badgley, M.B.; and Konkel, C.R.: User Needs, Benefits, and Integration of Robotic Systems in a Space Station Laboratory. (TBE-SSD-P601-89-191, Teledyne Brown Engineering Co.; NASA Contract NAS3-25278), NASA CR-185150, 1989.
- Hickman, J.M., et al.: Solar Electric Propulsion for Mars Transport Vehicles. NASA TM-103234, 1990.
- Huckelbridge, A.A.; and Abdallah, A.A.: Boundary Flexibility Method of Component Mode Synthesis Using Static Ritz Vectors. Computers and Structures, vol. 35, no. 1, 1990, pp. 51-61.
- Janetzke, D.C.; and Murthy, D.V.: Concurrent Processing Adaptation of Aeroelastic Analysis of Propfans. NASA TM-102455, 1990.
- Kielb, R.E.; and Ramsey, J.K.: Flutter of a Fan Blade in Supersonic Axial Flow. J. Turbomachinery, vol. III, no. 4, Oct. 1990, pp. 462-467.
- Ku, C.C.; and Williams, M.H.: Three Dimensional Full Potential Method for the Aeroelastic Modeling of Propfans. 31st Structures, Structural Dynamics and Materials Conference, Part 3, AIAA, 1990, pp. 1727-1735.
- Lawrence, C.; and Huckelbridge, A.A.: A Global Approach for the Identification of Structural Connection Properties. NASA TM-102502, 1990.
- Malachowski, M.J.: Beam Rider Module for an Articulated Robot Manipulator (ARM). Accurate Positioning of Long Flexible Manipulators. NASA CR-185151, 1990.
- Meeks, C.; DiRusso, E.; and Brown, G.V.: Development of a Compact, Lightweight Magnetic Bearing. AIAA Paper 90-2483, July 1990.
- Smith, T.E.: Aeroelastic Stability Characteristics of High Energy Turbines. Advanced Earth to Orbit Propulsion Technology 1990, NASA CP-3092-VOL-2, 1990, pp. 163-179.
- Smolinski, P.J.: Transient Finite Element Computations on the Transputer System. NASA CR-185199, 1990.
- Srivastava, R., et al.: Application of an Efficient Hybrid Scheme for Aeroelastic Analysis of Advanced Propellers. AIAA Paper 90-0028, Jan. 1990. (Also, NASA TM-102428).
- Structural Dynamics Branch Research and Accomplishments for FY 1989. NASA TM-102488, 1990.
- Yamamoto, O.; and August, R.: Structural and Aerodynamic Analysis of Large Scale Advanced Propeller Blade. AIAA Paper 90-2401, July 1990.

# REPORT DOCUMENTATION PAGE

*Form Approved  
OMB No. 0704-0188*

Public reporting burden for this collection of information is estimated to average 1 hour per response, including the time for reviewing instructions, searching existing data sources, gathering and maintaining the data needed, and completing and reviewing the collection of information. Send comments regarding this burden estimate or any other aspect of this collection of information, including suggestions for reducing this burden, to Washington Headquarters Services, Directorate for Information Operations and Reports, 1215 Jefferson Davis Highway, Suite 1204, Arlington, VA 22202-4302, and to the Office of Management and Budget, Paperwork Reduction Project (0704-0188), Washington, DC 20503.

<b>1. AGENCY USE ONLY (Leave blank)</b>			<b>2. REPORT DATE</b> November 1991		<b>3. REPORT TYPE AND DATES COVERED</b> Technical Memorandum		
<b>4. TITLE AND SUBTITLE</b>  Structural Dynamics Branch Research and Accomplishments for FY 1990			<b>5. FUNDING NUMBERS</b>  WU-505-63-5B				
<b>6. AUTHOR(S)</b>							
<b>7. PERFORMING ORGANIZATION NAME(S) AND ADDRESS(ES)</b>  National Aeronautics and Space Administration Lewis Research Center Cleveland, Ohio 44135-3191			<b>8. PERFORMING ORGANIZATION REPORT NUMBER</b>  E-5993				
<b>9. SPONSORING/MONITORING AGENCY NAMES(S) AND ADDRESS(ES)</b>  National Aeronautics and Space Administration Washington, D.C. 20546-0001			<b>10. SPONSORING/MONITORING AGENCY REPORT NUMBER</b>  NASA TM-103747				
<b>11. SUPPLEMENTARY NOTES</b>  Responsible person, Chuck Lawrence, (216) 433-6048.							
<b>12a. DISTRIBUTION/AVAILABILITY STATEMENT</b>  Unclassified - Unlimited Subject Category 39				<b>12b. DISTRIBUTION CODE</b>			
<b>13. ABSTRACT (Maximum 200 words)</b>  This publication contains a collection of fiscal year 1990 research highlights from the Structural Dynamics Branch at NASA Lewis Research Center. Highlights from the branch's major work areas—Aeroelasticity, Vibration Control, Dynamic Systems, and Computational Structural Methods—are included in the report as well as a listing of the fiscal year 1990 branch publications.							
<b>14. SUBJECT TERMS</b>  Aeroelasticity; Vibration control; Dynamic systems; Computational methods					<b>15. NUMBER OF PAGES</b> 43		
					<b>16. PRICE CODE</b> A03		
<b>17. SECURITY CLASSIFICATION OF REPORT</b> Unclassified		<b>18. SECURITY CLASSIFICATION OF THIS PAGE</b> Unclassified		<b>19. SECURITY CLASSIFICATION OF ABSTRACT</b> Unclassified		<b>20. LIMITATION OF ABSTRACT</b>	